JOC The Journal of Organic Chemistry

pubs.acs.org/joc Article

Characterization of Push−Pull-Type Benzo[X]quinoline Derivatives (X = *g* or *f*): Environmentally Responsive Fluorescent Dyes with Multiple Functions

Yasufumi Fuchi,*,§ Tomohiro Umeno,§ Yuichiro Abe, Keita Ikeno, Ryu Yamasaki, Iwao Okamoto, Kazuteru Usui,* and Satoru Karasawa*

Cite This: https://dx.doi.org/10.1021/acs.joc.0c01878 Read Online

ABSTRACT: Benzo[X]quinoline (X = *g* or *f*: **BQX**) derivatives bearing bis-trifluoromethyl and amine groups have been designed as push−pull-type fluorescent dyes. Through the synthesis of **BQX** derivatives from 2,7-diaminonaphthalene, linear-type (**BQL**) and angular-type (**BQA**) structural isomers were obtained. X-ray structures of single crystals from six given **BQX** derivatives revealed that the **BQL** and **BQA** series adopt planar- and bowl-shaped structures. In the fluorescence spectra, interestingly, the **BQL** series emitted in the near-infrared region over 700 nm in polar solvents. Based on the visible absorptions and base properties related to the amine moiety, the ammonia responsiveness was investigated using an ion-exchange reaction by the **BQX-HCl** salt. By exploiting the environmentally responsive fluorescence probe, cell imaging through confocal laser microscopy was conducted using HeLa and 3T3-L1 cells, emitting specific lipid droplets. The results indicate that **BQX** derivatives have multiple functions and may be applied in materials chemistry and biochemistry.

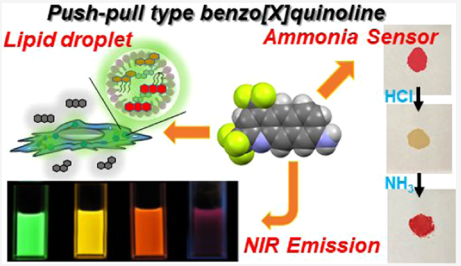

1. INTRODUCTION

Push−pull-type fluorescent dyes possessing electron-donor and -acceptor groups on π-conjugated rings have applications in materials chemistry and biochemistry.[1] For example, Prodan and dansyl analogs, which are well-known push−pull-type fluorescent dyes consisting of a bicyclic naphthalene framework,[2] yield electron spectra with solvatochromic behavior owing to photoinduced intramolecular charge transfer (PICT) in an excited state.[3] Solvent-dependent emission changes triggered by the PICT indicate the environmentally responsive characteristics of fluorescent dyes. Therefore, various fluorophores with push−pull-type fluorescent dyes have been used for applications as environmentally responsive fluorescent probes. In biochemistry,[4] Nile Red, which is composed of a polycyclic aromatic hydrocarbon, is a fluorescent cellular bioprobe and exhibits a bathochromic shift in polar solvents.[5] In addition to Nile Red, various fluorescent probes have been used for specific staining of lipid droplets (LDs) by utilizing their environmentally responsive properties.[6,7] LDs are composed of neutral lipids and are considered intracellular fat storage organelles.[8]

Additionally, quinoline analogs, such as quinine sulfate,[9] have been frequently used as bicyclic fluorophores.[10−12] Previous studies have also introduced bis-trifluoromethyl and amino groups on the quinoline ring, whereby fluorescent aminoquinoline derivatives (TFMAQ)[13] have been developed as fluorescent dyes (Scheme 1) that respond to various external stimuli such as solvent polarity,[13] heat,[13,14] light,[15] and mechanical stimuli.[14,16] Moreover, amine-responsive films with

Scheme 1. Molecular Structures of Fluorescent Benzoquinoline Derivatives[a]

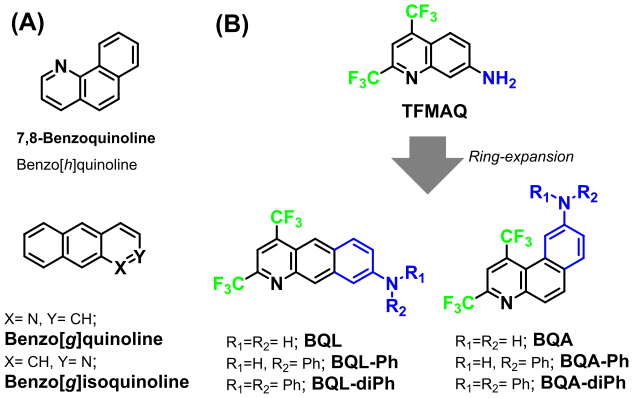

[a](A) Previous reported analogues; (B) TFMAQ and benzo[X]-quinoline derivatives (**BQL** series (X = *g*) and **BQA** series (X = *f*)) with electron-donor and -acceptor substituents on π-rings.

Received: August 4, 2020
Published: September 17, 2020

Scheme 2. Scheme for the Syntheses of BQL and BQA and Their Derivatives[a]

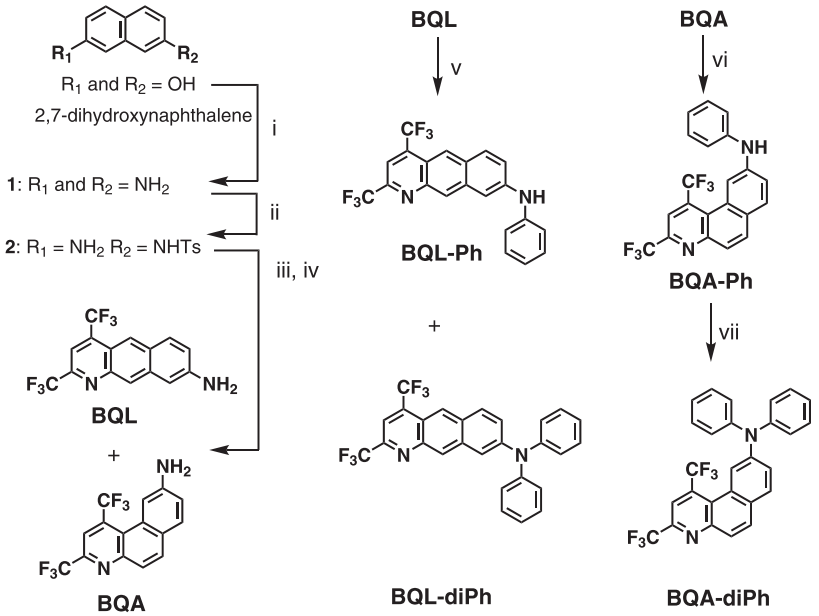

[a]Reagents and conditions: (i) $NaHSO_3$, 28% NH_3 aq., sealed tube, 170 °C, 92%; (ii) tosyl chloride, pyridine, rt, 75%; (iii) hexafluoroacetylacetone, montmorillonite K10, 1,4-dioxane, 60 °C; (iv) conc. H_2SO_4, 100 °C, 5% for **BQL** and 32% for **BQA**; (v) bromobenzene, $Pd(OAc)_2$, *t*-Bu_3P, *t*-BuOK, toluene, 100 °C, 31% for **BQL-Ph** and 38% for **BQL-diPh**; (vi) bromobenzene, $Pd(DPPF)Cl_2$, DPPF, *t*-BuOK, 1,4-dioxane, 100 °C, 62%; (vii) bromobenzene, $Pd(OAc)_2$, *t*-Bu_3P, *t*-BuOK, toluene, 100 °C, 99%.

absorption color change were developed as an amine sensor.[17] In addition to materials chemistry, there have been recent attempts to develop such materials for use in biochemistry. For example, specific fluorescence imaging of LDs with a greenish fluorescent color,[18] apoptosis-inducing reagents such as photosensitizers,[19] and thermoresponsive nanomaterials as *in vivo* tumor-imaging agents have been reported.[20]

The bicyclic framework needs to be expanded by aromatic rings to prompt the various forms of responsiveness at a lower energy and to obtain near-infrared spectra using push−pull-type compounds. In this study, we designed novel tricyclic benzo[X]quinoline (**BQX**) derivatives consisting of a ring-expanded TFMAQ framework. The tricyclic frameworks introduced with the electron push−pull groups are expected to show a red shift in the electron spectra. Various additional advantages, such as a large Stokes shift and an enhancement of fluorescence intensity compared to those without the push−pull groups, may be realized. In previous studies related to benzoquinoline analogs, a representative 7,8-benzoquinoline (benzo[*h*]quinoline) composed of the angular-type structural isomer (Scheme 1A) was investigated for use as a fluorescent dye.[21] However, the examination of the fluorescent dyes using linear-type **BQX** derivatives (benzo[*g*]quinoline[22] or benzo-[*g*]isoquinoline[23−25] in Scheme 1A) was limited because of the difficulty encountered in their selective synthesis. These **BQX** derivatives also emitted in the non-near-infrared region (<550 nm) in the solution. Through the introduction of push−pull-type substituents on the benzoquinoline ring, long-wavelength emissions (>650 nm) are expected. This paper reports on the syntheses, structural analyses, and photophysical properties of novel fluorescent benzo[*g*]quinoline (**BQL**) and benzo[*f*]-quinoline (**BQA**) derivatives, together with their phenyl-substituted derivatives (-Ph and -diPh). Ammonia responsiveness using an ion-exchange reaction of **BQX-HCl** salt was also examined, utilizing the strong visible absorptions and base properties. Finally, based on polarity-responsive fluorescence, intracellular fluorescence imaging of LDs in live cells was described for bioapplication.

2. RESULTS AND DISCUSSION

2.1. Synthesis. The scheme for synthesizing the **BQX** framework is shown in Scheme 2. According to a previous report,[26] the dihydroxyl group of 2,7-dihydroxynaphthalene was converted to the diamine group via the Bucherer reaction in the presence of sodium hydrogen sulfite under an aqueous ammonia solution into a sealed tube. Considering the low yield of the linear-type **BQL** derivative,[22−25] to increase the reaction yield of **BQL**, one amine group of compound **1** was selectively protected by a tosyl group, producing compound **2** with a 75% yield. Direct synthesis from compound **1** to **BQL** via Combes quinoline synthesis yielded the unexpected product **BQA** (23%). In contrast, **BQL** and **BQA** were obtained in 5 and 32% yields through a two-step synthesis from the protected **2** via an imine intermediate by Combes quinoline synthesis. From the viewpoint of the resonance energy between the phenanthrene (angular-type) and anthracene (linear-type) isomers,[27] the former was more stable than the latter, suggesting that the angular-type **BQX** is predominantly obtained via the Combes quinoline cyclization. Previous reports indicate that the linear-type **BQX** is the main product when concentrated sulfuric acid is used in the cyclization step.[28] Therefore, **BQL** synthesis requires further investigation to obtain a higher yield via kinetic control by considering factors such as orbital overlaps and functional groups. Modifications of amine groups by phenyl substitution via Buchwald−Hartwig cross-coupling were conducted in the presence of a Pd catalyst with a phosphine ligand. **BQL-Ph** and **BQL-diPh** were synthesized simultaneously in one batch in the presence of $Pd(OAc)_2$ using *t*-Bu_3P (catalyst A), obtaining 31 and 38% yields, respectively. Using a stepwise phenyl-

https://dx.doi.org/10.1021/acs.joc.0c01878
J. Org. Chem. XXXX, XXX, XXX−XXX

substituent reaction, **BQA-Ph** was prepared from **BQA** in the presence of $Pd(DPPF)Cl_2$ in 62% yield. Further, **BQA-diPh** synthesis was conducted from **BQA-Ph** using catalyst A in a quantitative yield. The molecular structures of **BQX** derivatives were characterized by nuclear magnetic resonance (NMR) spectroscopy, infrared (IR) spectroscopy, and electrospray ionization mass spectrometry (ESI).

2.2. X-ray Crystal Structure Analysis. The crystal structures of **BQX** derivatives were characterized by X-ray structure analysis. Single crystals suitable for X-ray analysis of all six **BQX** derivatives (**BQL, -Ph**, and **-diPh**, and **BQA, -Ph**, and **-diPh**) were obtained by recrystallization from various solvents. The molecular structures and Oak Ridge thermal ellipsoid plot (ORTEP) drawings with molecular packings are shown in Figures 1 and S1−S6. The crystallographic parameters and significant short contacts and angles are summarized in Tables 1 and S1−S4.

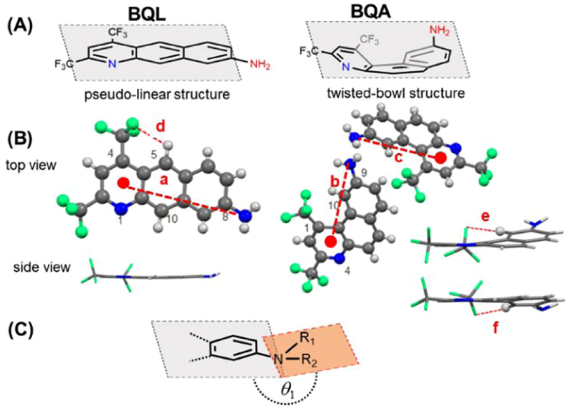

Figure 1. (A) Structural features of **BQL** and **BQA**; (B) top- and side-views of the crystal structures of **BQL** and **BQA**. Reddish broken lines indicate D−A distances between the centroids of pyridine rings and amine moieties, which were 7.4 and 6.3 Å for **BQL** (a) and **BQA** (b and c), respectively. Reddish dotted lines represent CH···F interactions of 2.49 (d), 2.19 (e), and 2.16 Å (f); (C) dihedral angles θ_1 between the fused Ph rings and amine moieties ($L_{Ph\text{-}NR1R2}$).

In the crystal structures of **BQL** and **BQA** (Figures 1, S1, and S4), the molecular twist based on the torsions of the **BQX** ring and the donor−acceptor (D−A) distances were considerably different. The torsion angles between a quinoline ring and the fused phenyl rings on the **BQX** rings ($L_{Q\text{-}Ph}$ in Table 1) were estimated at 2.4 and 6.3−6.4°, forming a pseudo-planar and a twisted bowl-shaped structure for **BQL** and **BQA**, respectively (Figure 1A,B). This twisted structure of **BQA** yielded the upward or downward forms frequently observed in benzo[*f*]quinoline derivatives.[29,30] Triggered by the bowl-shaped structure of **BQA**, the intramolecular short contacts between F and H atoms on C10 atoms were below 2.2 Å, which was shorter than the sum of the van der Waals radii (2.67 Å) (Figure 1B).[31] The corresponding distance in **BQL** was 2.41 Å (F−H at C5). The different isomers based on the benzo[X]quinoline framework (X = *g* or *f*) exhibited different D−A distances (between the donor and the acceptor moiety), which were estimated based on the distance between the centroid of the pyridine ring and the N atom of the amine moiety, yielding 7.4 and 6.3 Å for **BQL** and **BQA**, respectively (Figure 1B). The amine moieties adopted a pyramidal form, and the dihedral angles between the fused phenyl rings and the plane consisting of $L_{N\text{-}H\text{-}H}$ (Figure 1C) were estimated to be θ_1 = 23.4°, and 36.6 and 41.1° for **BQL** and **BQA**. This suggests that the amine of **BQL** contributes to a relatively high sp^2 hybrid character.[13] The 1.1 Å difference in the D−A distance and the sp^2 hybrid character may be responsible for the electron spectra in **BQX** derivatives and the base property (pK_a) at the amine moieties (*vide infra*). In terms of the packing of **BQL**, the H atoms on the amine moiety formed a long hydrogen bond with N1 (N···N: 3.34 Å) of the neighboring molecule, forming zigzag chains along the *c*-axis (Figure S1). The planar **BQL** molecule interacted with neighboring molecules by proximal $\pi-\pi$ stacking (3.40 Å), forming a head-to-head slipped-columnar fusion (Tables 1, S3, and Figure S1). For **BQA**, **BQA** formed zigzag chains with intermolecular hydrogen bonds at the N9 and N4 atoms of 3.10 and 3.27 Å along the *a*-axis, respectively. Furthermore, $\pi-\pi$ stacking with head-to-head slipped-columnar fusion (3.52 or 3.60 Å, Figure S4) was also observed with the twisted form.

Table 1. Selected Intramolecular Angles and Distances, and Significant Intermolecular Interactions

BQX (space group) and Z'	angle/deg: Q-Ph[a]	angle/deg: θ_1[b]	distance/Å: F−H[c]	distance/Å: D−A[d]	interactions (Å)[e]
BQL (*Fdd*2), Z' = 1	2.4	23.4	2.41	7.4	$\pi-\pi$ (3.40), HB (3.34)
BQL-Ph ($P2_1/c$), Z' = 1	1.6	2.82	2.52	7.4	$\pi-\pi$ (3.47), CH−n (2.60)
BQL-diPh (*C*2/*c*), Z' = 1	1.5	34.7	2.52	7.4	$\pi-\pi$ (3.76), F−F (2.94),
BQA ($P2_1$) Z' = 2	6.3, 6.4	36.6, 41.1	2.16, 2.19	6.3	$\pi-\pi$ (3.52, 3.60), HB (3.10, 3.27)
BQA-Ph ($P\bar{1}$) Z' = 1	7.5	16.8	2.18	6.3	$\pi-\pi$ (3.26-3.38), CH−n (2.74)
BQA-diPh ($P\bar{1}$) Z' = 1	8.9	33.4	2.18	6.3	$\pi-\pi$ (3.56), CH−π (2.68−2.83)

[a]Torsion angles between quinoline rings and fused phenyl rings ($L_{Q\text{-}Ph}$). [b]Dihedral angles between fused edged-phenyl rings in **BQX** and the amine moiety ($L_{Ph\text{-}NR1R2}$ in Figure 1C). [c]Between F atoms in CF_3 groups and H atoms (C5 atoms for **BQL** series and C10 atoms for **BQA** series). [d]Between the centroid in pyridine rings and N atoms in the amine moiety. [e]Significant intermolecular interactions for packing. HB, hydrogen bond; $\pi-\pi$, $\pi-\pi$ interaction; CH−n, CH−n interaction; F−F, F−F interaction; CH−π, CH−π interaction.

For the monophenyl-substituted **BQL-Ph** and **BQA-Ph** (Figures S2 and S5), the phenylamine moieties adopted syn conformations, wherein both derivatives formed a round shape. In peripheral amine moieties, through the decrease in dihedral angles (θ_1 = 2.82 and 16.8° for **BQL-Ph** and **BQA-Ph**), the planarity within the **BQX** rings was maintained ($L_{Q\text{-}Ph}$ = 1.6 and 7.5° for **BQL-Ph** and **BQA-Ph**). This yielded a higher sp^2 hybridization character compared to those of **BQL** and **BQA**. In the packings, the hydrogen bonds based on the secondary amine group were absent in both **BQX-Ph**. Instead of hydrogen bonds, CH−n interactions involving H atoms at the phenyl rings and the lone pair of N atoms in the pyridine rings were observed with 2.60 and 2.74 Å for **BQL-Ph** and **BQA-Ph**, respectively. Surprisingly, closed $\pi-\pi$ interactions of 3.26 and 3.38 Å with a head-to-tail fusion and the phenyl rings at the phenylamine moiety were observed in **BQA-Ph**, suggesting a strong electron effect in the electron spectra in the solid state (*vide infra*).

For the diphenylamine derivatives (**BQL-** and **BQA-diPh** in Figures S3 and S6), the dihedral angles of peripheral tertiary amine moieties were 34.7 and 33.4° for **BQL-diPh** and **BQA-**

https://dx.doi.org/10.1021/acs.joc.0c01878
J. Org. Chem. XXXX, XXX, XXX−XXX

diPh, suggesting that the contribution of sp^3 hybridizations of the amine moiety increased, and the donor effect of the phenyl rings may have diminished via twisting. In **BQA-diPh**, the torsion angle within the BQX rings had increased ($L_{Q\text{-}Ph}$ = 8.9°) compared to those in **BQA** (6.3 and 6.4°) and **BQA-Ph** (7.5°). The twisting of the **BQX** ring was also enhanced by an increase in the substitution number of the phenyl ring. Owing to the bulkiness of phenyl substitutions in the packing, the $\pi-\pi$ interactions had elongated to 3.76 and 3.56 Å, whereby multiple weak interactions such as CH−F, F−F, and F−H appeared.

The X-ray analyses provided insights into the differences in D−A distances, molecular twisting, and molecular packing. The 1.1 Å difference in the D−A distance between the **BQL** and **BQA** derivatives and the twisting difference of **BQX** rings may be the cause of the disparity in the donor effect in the ultraviolet−visible (UV−vis) spectra and the pK_a value, respectively. The packing differences may affect the differences in the solid electron spectra (Table 4 and Figure 5).

2.3. Photophysical Properties in Solution. The absorption and emission spectra of **BQL** and **BQA** were acquired in eight organic solvents: *n*-hexane (Hex), 1,4-dioxane (DOX), dibutylether (Bu_2O), chloroform ($CHCl_3$), ethyl acetate (AcOEt), *n*-butyl alcohol (BuOH), acetonitrile (MeCN), and methanol (MeOH). The absorption and emission spectra (excited at 450−480 nm for **BQL** and 400−420 nm for **BQA**), together with photographs of each solution (in Hex, $CHCl_3$, and AcOEt), taken under UV light (365 nm), are shown in Figures 2, 3A, and S7−S10. The resulting parameters including absorption or fluorescence maxima (λ_{max}^{abs} or λ_{max}^{fl}), molar absorption coefficient values (ε), absolute fluorescence quantum yields (ϕ^{fl}), and fluorescence lifetimes (τ) are summarized in Tables 2,3, and S5−S10. The radiative rate constants (k_r) and nonradiative decay constants (k_{nr}) were determined based on the given ϕ^{fl} and τ values, respectively.

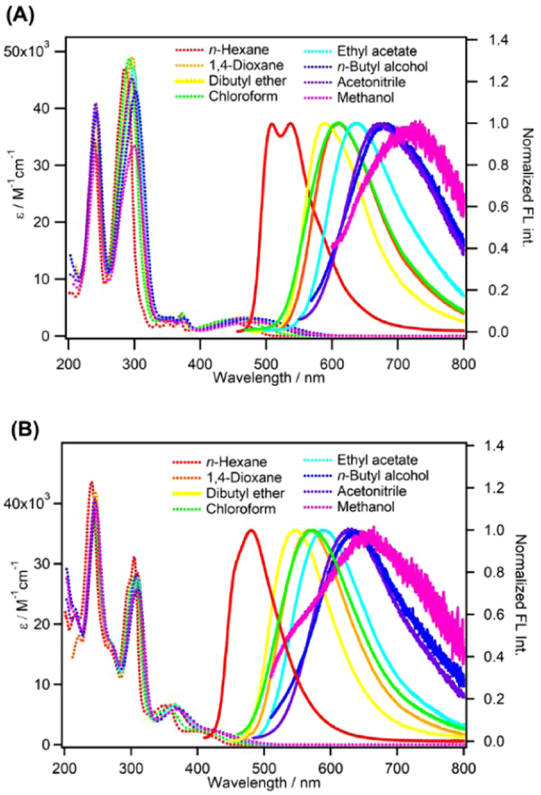

Figure 2. Emission (solid line) and absorption (dotted line) spectra of (A) **BQL** and (B) **BQA** in the given eight solvents.

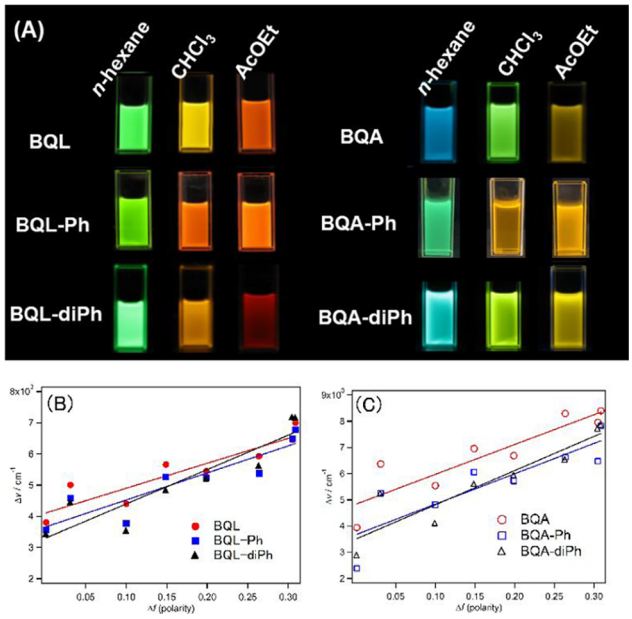

Figure 3. (A) Photographs taken under UV light (365 nm) in *n*-hexane, chloroform, and ethyl acetate. Lippert−Mataga plots of (B) **BQL** series and (C) **BQA** series. Circles, squares, and triangles represent **BQX**, **BQX-Ph**, and **BQX-diPh**, respectively. The solid lines are the least-squares fittings of each plot. Stokes shifts ($\Delta\nu$) and Δf values were calculated from $\nu_{max}^{fl} - \nu_{max}^{abs}$ (cm^{-1}) and $(\varepsilon - 1)/(2\varepsilon + 1)$-$(n^2 - 1)/(2n^2 + 1)$, respectively. ε and n represent the dielectric constant and refractive index, respectively.

In the absorption of BQL and BQA (Figure 2), broadened peaks over 400 nm with ε values between 2.0×10^3 and 3.0×10^3 were observed at the longest absorptions. The λ_{max}^{ab} values

Table 2. Photophysical Values of BQL and BQA Solutions (20 μM)[a]

	solvent	λ_{max}^{ab}	$\varepsilon \times 10^3$	λ_{max}^{fl}	Φ^{fl}	τ/ns	k_{nr}[b]
BQL	Hex	446	2.69	537	0.67	34.2	0.010
	DOX	468	3.34	610	0.09	6.41	0.14
	Bu_2O	467	2.99	588	0.16	9.17	0.092
	$CHCl_3$	452	3.00	607	0.07	3.87	0.24
	AcOEt	473	3.25	636	0.03	6.54	0.15
	BuOH	484	3.09	679	<0.01	n.d	
	MeCN	469	3.10	673	<0.01	n.d	
	MeOH	479	2.42	721	<0.01	n.d	
BQA[c]	Hex	404	2.19	481	0.10	4.65	0.19
	DOX	417	2.38	569	0.09	10.6	0.086
	Bu_2O	420	2.39	547	0.14	13.4	0.064
	$CHCl_3$	410	2.29	574	0.07	4.17	0.22
	AcOEt	423	2.43	589	0.05	5.25	0.18
	BuOH	417	2.55	627	0.01	0.95	1.0
	MeCN	418	2.41	638	<0.01	n.d.	
	MeOH	424	2.32	657	<0.01	n.d	

[a]The values of λ_{max}^{ab} and λ_{max}^{fl} are in nm. n.d., not detected. Excitation at a maximum of the corresponding excited spectra under individual conditions. [b]The k_{nr} values were calculated from $(1 - \varphi)/\tau$ (ns^{-1}). [c]λ_{max}^{ab} values were estimated using multipeak fitting.

https://dx.doi.org/10.1021/acs.joc.0c01878
J. Org. Chem. XXXX, XXX, XXX−XXX

Table 3. Selected Photophysical Data of BQL-Ph, BQL-diPh, BQA-Ph, and BQA-diPh in various solvents

	solvents	λ_{max}^{abs}/nm	ε^{a}	λ_{max}^{fl}/nm[b]	Φ^{fl}[c]
BQL-Ph	Hex	458	4.34	547	0.63
	$CHCl_3$	471	4.57	626	0.11
	AcOEt	478	4.72	638	0.05
	MeOH	489	4.98	731	n.d.
BQL-diPh	Hex	475	7.23	567	0.85
	$CHCl_3$	487	7.20	636	0.28
	AcOEt	483	6.44	644	0.18
	MeOH	485	6.59	743	n.d.
BQA-Ph[d]	Hex	422	2.22	494	0.10
	$CHCl_3$	433	2.08	587	0.09
	AcOEt	440	2.45	588	0.07
	MeOH	439	2.43	669	n.d.
BQA-diPh[d]	Hex	444	2.75	510	0.13
	$CHCl_3$	445	2.65	592	0.19
	AcOEt	442	2.96	599	0.12
	MeOH	442	2.82	677	n.d.

[a]The unit is $\times 10^3$ M^{-1} cm^{-1}. [b]Excitation at a maximum of the corresponding excited spectrum under individual conditions. [c]n.d., not detected. [d]λ_{max}^{ab} values were estimated by multipeak fitting.

of BQL (446−484 nm) were considerably longer than those of BQA (404−424 nm). These absorptions are attributed to the $S_0 \rightarrow S_1$ transitions, including a charge-transfer character based on the highest occupied molecular orbital (HOMO) → lowest unoccupied molecular orbital (LUMO) transition (*vide infra*). With the increase in solvent polarity, λ_{max}^{ab} showed a red shift based on positive solvatochromic behavior. The different λ_{max}^{ab} between BQL and BQA was a result of the twisted structure of the BQX rings. BQA, which possessed large torsion angles within the BQX ring, showed a short λ_{max}^{ab} owing to limited conjugation. In the fluorescence spectra, BQL had a longer wavelength emission (537−721 nm) compared to BQA (481−657 nm) as for the absorption spectra. As solvent polarity increased, the λ_{max}^{fl} of BQL showed a red shift. Interestingly, near-infrared emissions over 650 nm were observed in polar solvents such as BuOH, MeCN, and MeOH. In terms of the solvent dependence of the ϕ^{fl} values, BQL had a drastic decrease from a nonpolar (0.67) to a polar solvent (<0.01); however, BQA demonstrated only a small dependence in the nonpolar and medium-polar solvents (0.14 and 0.05).

In phenyl-substituted **BQL-Ph** and **BQL-diPh** (Figures S7 and S8; Tables 3, S6 and S7), there was a red shift in the absorption and emission spectra due to the donor effect of the phenyl rings. There was also a considerable increase in the ε values. As for **BQL**, the emission spectra in the polar solvents had near-infrared emissions around 700 nm. Through the substitution of two phenyl rings, the ϕ^{fl} values of **BQL-diPh** increased to 0.85 in nonpolar *n*-hexane compared to those of **BQL** and **BQL-Ph** (0.67 and 0.63). This enhancement in ϕ^{fl} resulted from the loss of the H atoms in the amine moiety and the substituted phenyl ring effect. In contrast, in **BQA-Ph** and **BQA-diPh** (Figures S9 and S10; Tables 3, S9, and S10), similar red shifts of absorption (with enhancement of ε values) and emissions were clearly observed. However, the near-infrared emission over 700 nm was absent even for **BQA-diPh**. For the ϕ^{fl} of **BQA-diPh**, a subtle increase in Hex was observed (0.13) owing to the loss of the NH group, compared to **BQA** and **BQA-Ph** (0.10). These results suggest that, as opposed to polarity dependence, another essential nonradiative decay process may be present in the **BQA** series. The observed fluorescence quenching in polar solutions (especially in **BQL** series) and the positive solvatochromic behavior may be caused by the stabilization of the PICT state in the excited state[17,32] for typical push−pull-type fluorophores.

To quantitatively elucidate the photophysical properties according to Lippert−Mataga plots,[13,17,33] the Stokes shift ($\Delta\nu$, cm^{-1}) values were plotted as a function of solvent polarity (Δf) (Figure 3B,C). From the slope of the linear fitted lines, the difference in the dipole moment between the ground and excited states ($\Delta\mu$) was determined using eq 1

$$\Delta\nu = \frac{2\Delta\mu^2}{hca^3}\Delta f + \text{constant} \quad (1)$$

where h and c are Planck's constant and the velocity of light, respectively, and a is the Onsager radius of the molecule. The radii of **BQL** and **BQA** were 4.50 and 4.14 Å, respectively, as estimated from the density-functional theory (DFT) calculations.[34] In the plots, a positive correlation between Δf and $\Delta\mu$ was observed in the same manner as for TFMAQ.[13] The estimated $\Delta\mu$ values for **BQL** and **BQA** were 8.5 and 9.0 Debye (D), respectively (slightly higher than that of TFMAQ (8.1 D)),[13] indicating that **BQA** is significantly influenced by solvent polarity in the excited state. The D−A distances of **BQL** and **BQA** estimated by X-ray analysis were 7.4 and 6.3 Å (Table 1), respectively, with shorter D−A distances being expected to produce larger $\Delta\mu$ values. The phenyl-substituted species, **BQL-Ph** (a = 4.68 Å), **BQL-diPh** (a = 4.86 Å), **BQA-Ph** (a = 4.59 Å), and **BQA-diPh** (a = 4.68 Å), yielded $\Delta\mu$ values of 9.4, 11.2, 10.6, and 11.5 D, respectively. The $\Delta\Delta\mu$ values ($\Delta_{BQX\text{-}diPh} - \Delta_{BQX\text{-}Ph}$) were 1.8 and 0.9 for **BQL** series and **BQA** series, respectively. This suggests that the donor effect of the phenyl ring of the **BQA** series was limited owing to the twisting of the **BQA** rings (Table 1).

The fluorescence decays of **BQL** and **BQA** in various solutions were traced, and τ values were obtained using first-order decay analysis (Figures S11−16 and Tables 2, S5, S8). In the nonpolar Hex solution, the τ value of **BQL** was notably larger (34.2 ns) than that of **BQA** (4.65 ns). As the solvent polarity increased, the τ of **BQL** decreased, accompanied by a reduction in ϕ^{fl} and an emission red shift. In contrast, the solvent dependence of τ for **BQA** was smaller than that for **BQL**. The nonradiative decay constants (k_{nr}) were determined based on the given τ and ϕ^{fl} of **BQL**, according to the relationship $(1 - \phi^{fl})/\tau$, yielding a strong solvent dependence (0.010−0.22 ns^{-1} in Hex, DOX, Bu_2O, $CHCl_3$, and AcOEt). This result suggests that nonradiative decay of **BQL** is regulated by the polarity surrounding the fluorophores; this means that the PICT transition is stabilized by more polar solvents for fluorescent molecules bearing donor−acceptor groups. In contrast, the k_{nr} of **BQA** yielded a subtle solvent dependence (0.064−0.22 ns^{-1} in Hex, DOX, Bu_2O, $CHCl_3$, and AcOEt), suggesting the presence of another decay process. One possible route for the decay process in **BQA** is energy loss due to the rapid conformational change related to the twisted **BQX** rings. This means that the nonplanar twisted-**BQA** ring may move up or down triggered by heat; these conformers would be in equilibrium in the solution under ambient conditions (Figure 4). To confirm the earlier hypothesis, variable-temperature (VT) NMR was conducted for **BQA** in CD_2Cl_2 from 20 to −80 °C (Figure S17). Upon lowering the temperature, a remarkable upfield-shift in the resonance of H^{10}

https://dx.doi.org/10.1021/acs.joc.0c01878
J. Org. Chem. XXXX, XXX, XXX−XXX

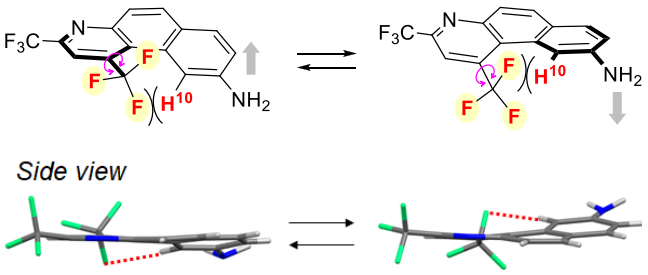

Figure 4. Proposed equilibrium between twisted-**BQA** conformers in the solution state. Bottom figures are the side-views obtained by X-ray structures with dotted reddish lines (CH···F interactions by 2.16 Å).

and a subtle upfield-shift for H^6 were observed. Based on X-ray analysis, the H^{10} atom in the twisted-**BQA** interacted with the F atom to form a CH−F interaction. In the solution state at 23 °C, the validity of the CH−F interaction should diminish owing to the rapid rotation of the CF_3 groups, causing the upfield-shift of the proton.[35] However, the corresponding proton was observed at 7.90 ppm at 23 °C from 7.82 ppm at −80 °C, exhibiting a downfield-shift with increasing temperature. This discrepancy between the chemical shifts can be explained as the resonance effect of the **BQA** ring becoming dominant with increasing temperature; i.e., at lower temperatures, the conformational change in **BQA** became slow to adopt the twisted form, reducing the contribution of the resonance effect. At that time, the corresponding proton showed an upfield-shift. In contrast, with increasing temperature, the **BQA** ring can quickly move up and down, enhancing the contribution of the resonance effect and thus resulting in the downfield-shift of the proton. For **BQL** (Figure S18), although the CH−F interaction was negligible in the X-ray structure (Table 1), a gentle upfield-shift of the corresponding H^5 proton was observed with decreasing temperature. The result suggests that the dominant contribution to the chemical shift is not the CH−F interaction but the alteration of the resonance effect in the **BQX** ring. Moreover, these results suggest that the conformational change between the twisted conformers is responsible for the fluorescence quenching based on a nonradiative decay process.

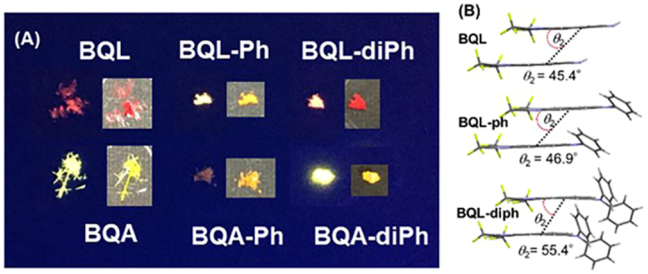

Figure 5. (A) Images of crystalline samples taken under room and UV lighting (365 nm); (B) angles (θ_2) between $\pi-\pi$ stackings of the **BQL** series with head-to-head slipped-columnar fusion.

2.4. Photophysical Properties in the Solid State. In solution conditions, the **BQX** derivatives exhibited visible absorption and fluorescence color with moderate ε and ϕ^{fl} values. In addition, the bicyclic TFMAQ derivatives emitted in the visible region with moderate ϕ^{fl} even in the solid state.[13−15] As such, investigations of photophysical properties in the solid state for tricyclic **BQX** derivatives were conducted. The resulting absorption and fluorescence spectra of **BQX** derivatives in the solid state are shown in Figure S19, and images under room and UV lighting are shown in Figure 5A. The photophysical parameters are summarized in Table 4. In

Table 4. Photophysical Parameters of BQX Derivatives in the Solid State

	λ_{max}^{ab}/nm[a]	λ_{max}^{fl}/nm	Φ^{fl}	$\pi-\pi$ stacking distance/Å[b]	$\pi-\pi$ stacking θ_2/deg[c]
BQL	552	613	0.01	3.40	45.4
BQL-Ph	510	585	0.06	3.46	46.9
BQL-diPh	543	625	0.01	3.70	55.4
BQA	423	545	0.06	3.52, 3.60	
BQA-Ph	440	575	0.03	3.27	
BQA-diPh	459	542	0.26	3.56	

[a]Diffuse-reflectance method with conversion using a Kubelka−Munk function using diluted KBr samples. [b]See Table 1. [c]$\pi-\pi$ stacking angles in Figure 5B.

contrast to the solution samples, the λ_{max}^{ab} values of the **BQL** series were strongly dependent on the crystal structures,[13−15] as opposed to the number of phenyl rings. This yielded the λ_{max}^{ab} values with the order **BQL** > **BQL-diPh** > **BQL-Ph**. In the X-ray crystal structure, **BQL** crystallized with the highest density (1.724 g/cm^3 in Table S1) and with the shortest $\pi-\pi$ stacking distance between **BQX** rings (Table 4), suggesting that **BQL** exhibited the longest λ_{max}^{ab} and the second longest λ_{max}^{fl} among the **BQL** series. However, owing to the strong intermolecular hydrogen bond and the close $\pi-\pi$ stacking, a considerably small ϕ^{fl} was obtained (<0.01) based on aggregation-induced quenching.[36] Despite **BQL-diPh** carrying two phenyl rings, there was limited red shift of λ_{max}^{ab} and λ_{max}^{fl}. The $\pi-\pi$ stacking angles (θ_2 in Figure 5B) among the head-to-tail columnar packings were estimated to be 45.4, 46.9, and 55.4° for **BQL**, **BQL-Ph**, and **BQL-diPh**, respectively (Figure 5B). The largest θ_2, 55.4°, in **BQL-diPh** was larger than 54.7°, indicating the behavior at the borderline between *J* and *H*-aggregation.[37] This means that **BQL** and **BQL-Ph** crystallized with *J*-aggregation (<54°), whereas **BQL-diPh** crystallized with *H*-aggregation (>54°), resulting in a blue shift of absorption accompanied by weak emission. Accordingly, the solid **BQL-diPh** absorbed and emitted with a limited red shift, together with a small ϕ^{fl} value. In contrast, the λ_{max}^{ab} of the **BQA** series was dependent on the number of phenyl rings. However, the λ_{max}^{fl} and ϕ^{fl} values were dependent on the crystal packings. The monophenyl **BQA-Ph** emitted with the longest wavelength and the smallest ϕ^{fl} values because of its shortest $\pi-\pi$ stacking distance (3.27 Å) among the **BQA** series. Diphenyl **BQA-diPh** emitted the shortest wavelength and the highest ϕ^{fl} value because of its missing hydrogen bond, long $\pi-\pi$ stacking distance (3.50 Å), and the largest angle ($L_{Q\text{-}Ph}$ = 8.9° and θ_1 = 33.4° in Table 1), which were related to the twisted **BQX** ring and the amine moiety.

2.5. Computational Chemistry. DFT calculations were performed to support the electronic states of **BQX** derivatives using theoretical calculations. The initial geometries of molecules obtained by X-ray analysis were optimized at the B3LYP/6-31G** level. Tamm−Dancoff (TD)-DFT, incorporating the TD approximation calculations of the molecules for UV−vis spectra, was conducted at the B3LYP/6-311G** level of theory. In the HOMO and the LUMO of **BQL** (Figure 6A), the orbitals were distributed over all of the atoms of the **BQX**

https://dx.doi.org/10.1021/acs.joc.0c01878
J. Org. Chem. XXXX, XXX, XXX−XXX

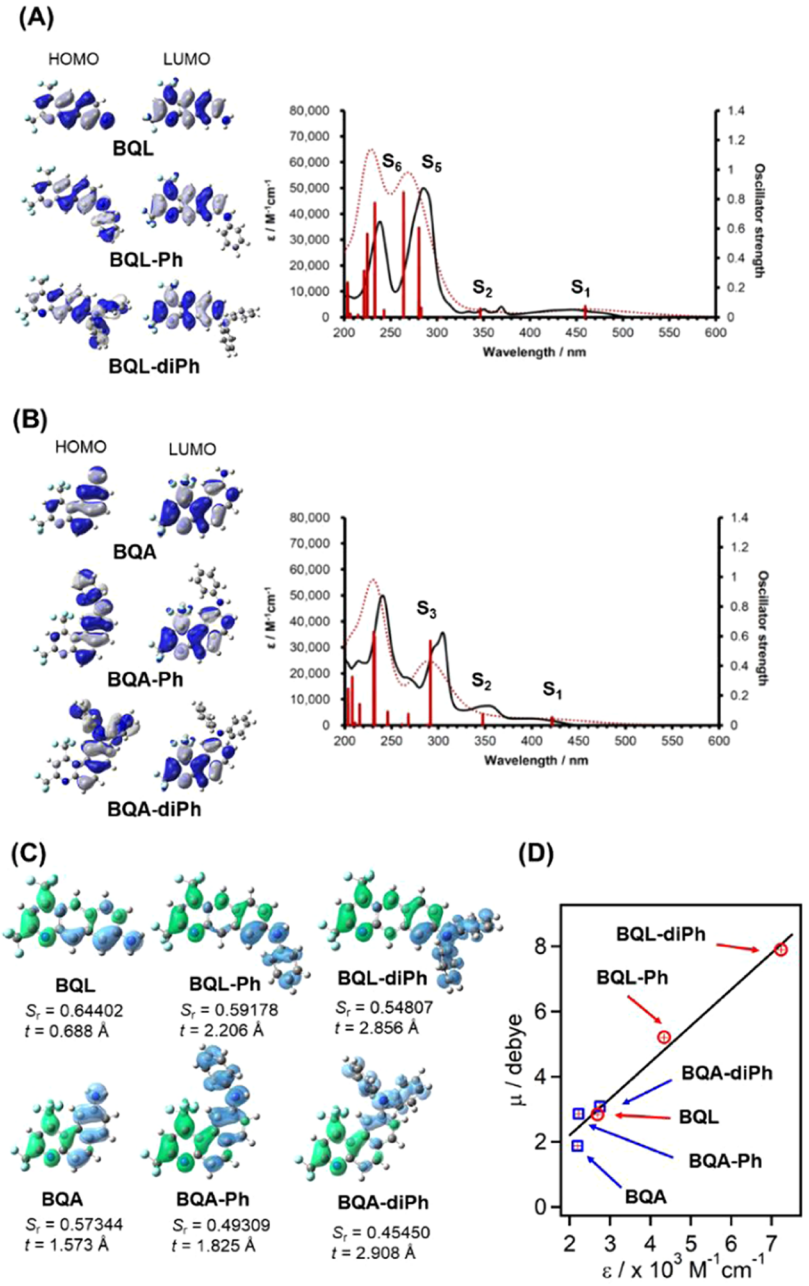

Figure 6. Left panels in (A, B): graphical representations of the highest occupied and the lowest unoccupied Kohn−Sham orbital (isovalue = 0.02) of (A) **BQL** and (B) **BQA**. Right panels indicate UV−vis spectra (*n*-hexane: black solid lines) together with the calculated spectra (reddish broken lines) by TD-DFT for (A) **BQL** and (B) **BQA**. (C) Electron density difference between the ground and the first excited state ($\Delta\rho(r) = \rho^{ES}(r) - \rho^{GS}(r)$) with S_r and t indices. Bluish and greenish surfaces represent positive and negative regions, respectively (isocontour value = 0.01). (D) Correlation plot between the transition dipole moments (μ) and the given ε values at the longest wavelength of all **BQL** derivatives ($R^2 = 0.997$).

ring, with the exception of the CF_3 groups in the HOMO. However, the orbitals tended to be distributed at the amine moiety (donor) in the HOMO and at the quinoline ring (acceptor) in the LUMO. For **BQA** (Figure 6B), there was a clear deviation of the molecular orbital (MO) distributions between the HOMO and LUMO. In the HOMO, the MOs were almost completely distributed around the amine moiety, while an absence of MO around the quinoline ring with CF_3 groups was observed. In the LUMO, the MOs tended to be distributed around the pyridine ring, as opposed to the amine moiety. These results suggest that **BQA** readily undergoes charge separation between the HOMO → LUMO transition compared to **BQL**. With an increase in the number of phenyl rings, there was a larger deviation of the MO distribution between the electron-donor and -acceptor groups (Figure 6A,B). For quantitative analysis, the numbers of contributions of a hole and an electron contained in the individual MOs were revealed. In the HOMO and LUMO, the contributions of **BQL** (Figures S20−S22) and **BQA** (Figures S23−S25) were estimated at 96.3 and 96.5% based on the hole and at 95.0 and 96.0% based on the electron, respectively. This indicates that the charge separation occurs mainly between the HOMO → LUMO transition in both derivatives. To evaluate the relationship between the amplitude of charge separation and the structures of the **BQX** derivatives, using the Multiwfn program,[38] the S_r and t indices[38,39] were estimated to be 0.644

https://dx.doi.org/10.1021/acs.joc.0c01878
J. Org. Chem. XXXX, XXX, XXX−XXX

a.u. and 0.688 Å for **BQL** and 0.573 a.u. and 1.573 Å for **BQA**, respectively (Figures 6, S26, S27, and Table S12). The lower S_r[40] and higher t indices[41] mean a larger charge separation; **BQA** causes a larger charge separation compared to **BQL**. This result agrees with the $\Delta\mu$ values (8.5 and 9.6 D for **BQL** and **BQA** in Figure 3A, respectively). This indicates that the contribution of the charge separation in the excited state for **BQA** is larger than that for **BQL**. Moreover, the results correlate with the D−A distance from X-ray analysis. The distance between the centroid in the fused-pyridine ring and the amine moiety was considered the D−A distance, yielding 7.4 and 6.3 Å for **BQL** and **BQA**, respectively (Table 1). These results were supported by the q_{ct} index[42] using the program Gaussian (Figures S26, S27, and Table S12). For the phenyl-substituted **BQX**, there was a similar change across all indices (S_r, t, and q_{ct}) as the number of phenyl rings increased. This suggests that the charge separation was accelerated by phenyl substitution (Figure 6C and Table S12).

TD-DFT calculations were performed (Figure 6 in the right panels) to reproduce the UV−vis absorptions (Figure 2). The longest broadened absorptions at 456 and 404 nm (*n*-hexane) for **BQL** and **BQA** were assigned as the $S_0 \rightarrow S_1$ transition (f = 0.074 and 0.053 for **BQL** and **BQA**, respectively) based on the HOMO → LUMO transition. The broadened shapes were also reproduced. In addition to the longest absorptions, all other absorptions were assigned (Figure 6 and Table S11). The calculated transition dipole moment (μ) linearly correlated with the ε values of the **BQX** derivatives (Figure 6D and Table S12).

2.6. Exploiting as an Ammonia Sensor. The amine moieties in the **BQX** framework possess roles as an electric donor effect and as an acidic response. Utilizing the strong visible absorptions (ε = 2.0−3.0 × 10^3) based on the D−A effect and acid−base reactivity, the ammonia responsiveness of solid **BQX-HCl** salts (Figure 7A) was investigated. The base properties of **BQL** and **BQA** were assessed to estimate their pK_a values in HCl solutions (<pH 2) and McIlvaine buffer solutions[43] (>pH 2) containing citric acid and disodium phosphate (Figure S27). The pK_a values were 1.8 and 2.2 for the protonated-**BQL** and **BQA**, respectively, indicating that **BQA** possesses a stronger base property than **BQL** and TFMAQ (pK_a = 0.9 for the protonated TFMAQ). The different basicities between protonated-**BQL** and -**BQA** are a result of the length of the π-conjugation system and the reduction in the electron-withdrawing effect by the CF_3 group; **BQA** consists of a shorter π-conjugation system owing to its twisted bowl-shaped structure, producing a λ_{max}^{ab} that is shorter than that for **BQL** (Table 2). Moreover, its MOs are more localized at the amine moiety in the HOMO, compared to that of **BQL** (Figure 6A,B). Under a closed HCl atmosphere prepared using 33% HCl solution, the color of the exposed **BQX** changed gradually, exhibiting a pale-brownish solid from a reddish solid for **BQL** (Figure 7B) and a colorless solid from a yellowish solid for **BQA** (Figure 7C). These color changes were confirmed by the absorption spectra, and the corresponding round maxima at 500 and 450 nm decreased to yield the corresponding HCl salts through an acid−base reaction. The production of HCl salts was also confirmed by IR spectra (Figure S28). Surprisingly, the HCl salts rapidly reacted with NH_3 gas prepared using 28% NH_3 solution, such that the color change was reversed. At this time, via the ion-exchange reactions, the production of NH_4Cl salt was observed in the IR spectra (Figure S28). This quick responsiveness and

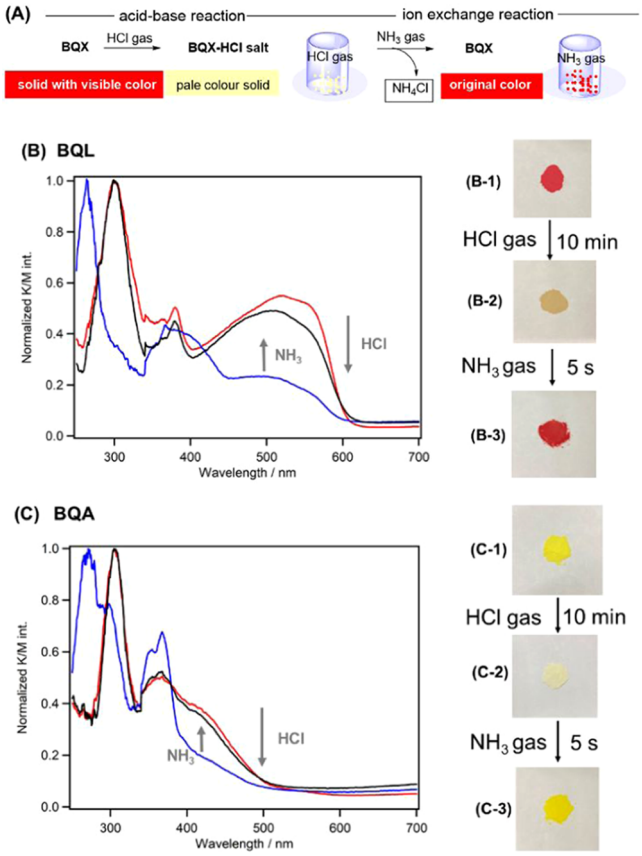

Figure 7. (A) Schematic of an ammonia sensor taking advantage of the acid−base reaction between **BQX** and HCl and the ion-exchange reaction between **BQX-HCl** and NH_3; (B, C): solid-state spectral changes and photographs before and after exposures to HCl gas and NH_3 gas for (B) **BQL** and (C) **BQA** diluted by KBr (2 wt %). In the spectra, reddish, bluish, and black solid lines represent **BQX** after exposure to HCl and the resulting **BQX-HCl** after exposure to NH_3 gas. In the photographs, top (B or C-1), middle (B or C-2), and bottom (B or C-3) panels represent **BQX** after exposure to HCl gas for 10 min and the resulting **BQX-HCl** salt after exposure to NH_3 gas for 5 s.

color change accompanied by a large difference in absorption before and after the exposure processes indicate that **BQX-HCl** salts may behave as ammonia sensors. Additionally, **BQX-HCl** salts are capable of being exploited as an alternate Kaiser test,[44] which is frequently used in peptide syntheses.[45]

2.7. Fluorescence Imaging in Live Cells. As per the observed fluorescence properties, the **BQX** derivatives fluoresce with moderate quantum yields in nonpolar environments, and quenching occurs in polar environments such as aqueous solutions. This molecular property enables specific detection of nonpolar environments with a high signal-to-noise ratio (SNR) in biological systems. Based on the greenish fluorescence of LDs obtained using TFMAQ analogs,[13] the **BQ** derivatives were applied as a reddish fluorescent staining reagent for LDs in live cells (Figure 8A). Cultured HeLa cells were stained with **BQL** or **BQA** and costained with LipidTOX Deep Red (Life Technologies),[46] an established probe for neutral lipids[43] (Figure 8C,D). Cells were incubated with 10 μM **BQL** or **BQA** in a culture medium, and fluorescence imagery was obtained using confocal laser microscopy without washout (extinction/emission (Ex/Em) = 488/595 nm for **BQL**, Ex/Em = 403/525 nm for **BQA**, Ex/Em = 637/700 nm

https://dx.doi.org/10.1021/acs.joc.0c01878
J. Org. Chem. XXXX, XXX, XXX−XXX

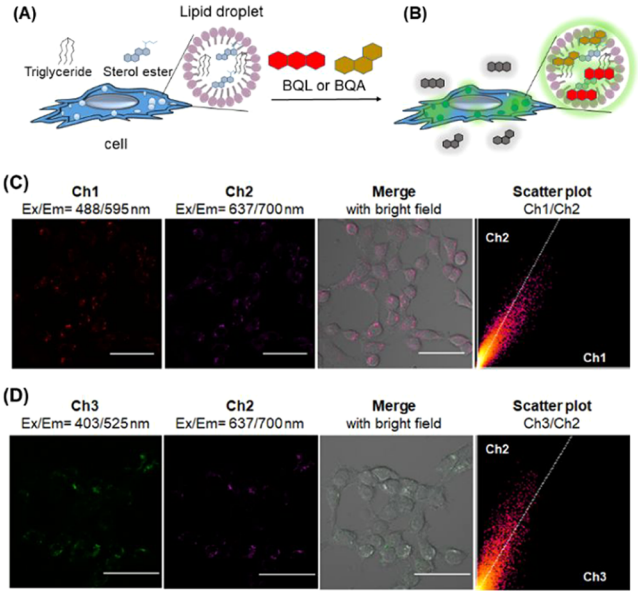

Figure 8. (A, B): Schematic of cell fluorescence imaging using **BQX**. (A) Cell with an enlarged lipid droplet (LD) before treatment with **BQX**; (B) LD fluorescence imaging after incubation with **BQX**. **BQX** incorporated into LD is represented by a strong emission color. Unincorporated **BQX** shows a dark color. (C, D) Fluorescence images and corresponding scatter plots of HeLa cells acquired by confocal laser microscopy. Fluorescence staining was conducted using (C) **BQL** or (D) **BQA** (10 μM in a culture medium) and LipidTOX Deep Red costain. *R* values (Pearson's correlation coefficient) were (A) 0.92 and (B) 0.83 for each scatter plot. Scale bars are 50 μm.

for LipidTOX Deep Red). In the fluorescence imageries for **BQL**, **BQA**, and LipidTOX, a granular collection of fluorescent regions was observed in the cells. The fluorescence imageries obtained after treatment with **BQL**, **BQA**, and LipidTOX were analyzed using scatter diagrams and Pearson's correlation coefficient[47] to assess the similarities between the distributions of **BQX** and LipidTOX. The R values for **BQL** and **BQA** were 0.92 and 0.83, respectively. This indicates the colocalization of **BQXs** with LipidTOX in LDs in living HeLa cells. Therefore, **BQX** may be used as red-colored probes for fluorescence imaging of LDs in living cells by exploiting their specific fluorescence in hydrophobic environments. Notably, **BQL** is capable of detecting LDs at longer fluorescence wavelengths (lower energies) than the TFMAQ-8Ar series[18] (Ex/Em = 403/525 nm) that has previously been reported. To date, several probes with red-colored fluorescence for LD imaging have been reported.[6,7] In comparison, **BQL** has a relatively large Stokes shift and significantly higher SNR between nonpolar (e.g., ϕ^{fl} = 0.67 in Hex) and polar (e.g., ϕ < 0.01 in MeOH) environments. From the confocal laser microscopy fluorescence imaging of HeLa cells, fluorescence imagery and emission spectra of **BQL** and **BQA** within cells and the intracellular matrix were obtained at various wavelengths (Figures S29–S31). As shown by the images acquired with **BQL**, potent fluorescence signals excited at 488 nm were collected from 560 to 660 nm, resulting in intracellular emission with a peak at 610 nm (Figure S31A). This suggests that the polarity of the LDs of HeLa cells is lower than that of the AcOEt solution and higher than that of the $CHCl_3$ solution (Table 2). The polarity of the LDs of MCF7 cells has previously been reported[48] to be between those of AcOEt and *n*-butyl acetate, consistent with these results for HeLa cells. In addition, the intracellular spectrum of **BQA** (Figure S31B) yielded an emission maximum at approximately 550 nm, indicating that its polarity is between those of chloroform and ethyl acetate, consistent with the **BQL** results.

The cytotoxicities of **BQL** and **BQA** were subsequently investigated to determine whether the compounds are appropriate for live-cell imaging (Figure S32). The cytotoxicity toward HeLa cells incubated with each compound for 2 h at 37 °C was evaluated using the MTS reagent (3-(4,5-dimethylthiazol-2-yl)-5-(3-carboxymethoxyphenyl)-2-(4-sulfophenyl)-2*H*-tetrazolium), which is a water-soluble tetrazolium salt. After incubation with high concentrations (100 μM) of **BQL**, the MTS assay demonstrated cell viability of over 70%, showing that **BQL** has low cytotoxicity. In contrast, a cell viability of less than 30% was obtained after incubation with 100 μM of **BQA**, indicating its high cell-growth inhibiting activity for HeLa cells. The difference in cytotoxicity between **BQL** and **BQA** may be attributed to the structure of the **BQ** unit fused to the TFMAQ framework (linear or angular). Pyrido carbazole derivatives[19] fused to TFMAQ with angular-type structures have previously been shown to possess high cytotoxicity. Furthermore, the photostabilities of **BQL** and **BQA** in methanol solution (20 μM) were examined under irradiation by light generated with a high-pressure mercury lamp. The resulting values were compared with the photostability of Nile Red, a fluorescent probe commonly utilized for LDs (Figure S33). The photostabilities were evaluated on the basis of the degradation of corresponding absorption peaks. The decay of Nile Red was the most rapid, whereas **BQL** showed a more moderate decay than **BQA**, indicating that photostability had the order **BQL**> **BQA**> Nile Red. Considering the emission color, cytotoxicity, and photostability, **BQL** is more suitable for fluorescence imaging of LDs in live cells than **BQA**. Fluorescence imaging of LDs was then conducted in differentiated 3T3-L1 adipocytes[49] stained with the three **BQL** derivatives synthesized in this study (Figure S34). The differentiated cells were incubated with 5 μM of each compound in the culture medium, and the fluorescence images were tracked by confocal laser microscopy without washout (Ex/Em = 488/595 nm). In **BQL**-stained images (Figure S34A), specific fluorescence signals in differentiated 3T3-L1 cells were observed, revealing spherical clusters of LDs. In contrast, signals were absent in the images obtained with **BQL-Ph** and **BQL-diPh** (Figures S34B,C). It is possible that **BQL-Ph** and **BQL-diPh** exhibited no fluorescence within the cells because of the high hydrophobicity of the phenyl groups, preventing a homogenous distribution of molecules in the aqueous cellular environment. A TFMAQ-8Ar derivative with hydrophobic *tert*-butyl groups has previously been reported to not incorporate well into the LDs in differentiated 3T3-L1 cells.[17] Thus, among the **BQ** derivatives developed in this study, **BQL** is the most suitable probe for fluorescence imaging of LDs.

3. CONCLUSIONS

Push–pull-type tricyclic benzo[X]quinoline (X = *g* and *f*) derivatives bearing donor and acceptor groups were newly prepared as conformational isomers consisting of linear-type (**BQL**) and angular-type (**BQA**) structural isomers. To enhance the electron-donor effect, the phenyl group was introduced into the amine groups; a total of six derivatives were prepared as environmentally responsive fluorescent dyes. In X-ray analyses, the **BQL** series adopted pseudo-planar

https://dx.doi.org/10.1021/acs.joc.0c01878
J. Org. Chem. XXXX, XXX, XXX–XXX

structures, whereas the **BQA** series exhibited twisting of the benzoquinoline ring with torsion angles of 6.3−8.9°. In the crystal packings, the **BQL** series crystallized with head-to-head slipped-columnar fusion. In the **BQA** series, the three individual derivatives crystallized with different fusions. In the electron spectra, the **BQL** series emitted relatively strongly in nonpolar solutions and in the near-infrared region over 700 nm for polar solutions. This near-infrared emission is the longest wavelength among the benzoquinoline derivatives previously reported.[22−25] In contrast, the **BQA** series emitted weakly compared to the **BQL** series owing to the vibrations attributed to the upward and downward twisted-rings. In the Lippert−Mataga plots, the twisted-**BQA** series possessed higher $\Delta\mu$ values compared to those of the **BQL** series, indicating that the charge separation in the excited state was larger than that in the **BQL** series. In the solid spectra, absorption and emission were considerably controlled by the crystal packings. In particular, the $\pi-\pi$ stacking distance significantly impacted the ϕ^{fl} values; the highest and lowest ϕ^{fl} were from **BQA-diPh**, which possesses the longest $\pi-\pi$ stacking distance, and **BQA-Ph**, which possesses the shortest $\pi-\pi$ stacking distance, respectively. The ammonia responsiveness was investigated using **BQX-HCl** salt by utilizing the relatively strong visible color and base properties. It resulted in a rapid responsiveness toward NH_3 gas by an ion-exchange reaction. The LDs in living cells were stained with reddish fluorescence without a washout by utilizing the environmentally responsive fluorescence properties of **BQL**. The results indicate that **BQX** derivatives have applications in materials chemistry and biochemistry. To enhance their multifunctionality, molecular designs are under investigation involving changing substituents and the π conjugation system.

4. EXPERIMENTAL SECTION

4.1. General Information. ^{1}H, ^{13}C, and ^{19}F NMR spectra were measured by a Bruker Biospin AVANCE II 600 or III 300 spectrometer using $CDCl_3$ as the solvent. VT-NMR spectra were recorded by JEOL JNM-ECZ400S in CD_2Cl_2. Infrared spectra for tableting samples with KBr were recorded using a JASCO FT-IR spectrometer. High-resolution electrospray ionization mass spectra were recorded using a JEOL JMS-T 100LP spectrometer. UV−Vis spectra in solutions were recorded using JASCO V760 spectrometers. UV−Vis spectra in solid states were recorded using JASCO V570 spectrometers equipped with a calibrated integrating sphere system. The fluorescence spectra and quantum yields of solutions and solids were recorded on a JASCO FP-8500 spectrofluorimeter equipped with a calibrated integrating sphere system. The fluorescence decay plots were recorded by HORIBA FluoroCube.

4.2. Synthesis Procedure. *4.2.1. 2,7-Diaminonaphthaline (**1**).*[26] A mixture of 2,7-dihydroxynaphthaline (2.00 g, 12.5 mmol) and $NaHSO_3$ (5.20 g, 50.0 mmol) in 28% ammonia solution (100 mL) was placed in a pressure reactor. The reaction mixture was sealed and heated to 170 °C (500 rpm) in a heating block. After being stirred for 9 h, the reaction mixture was cooled to room temperature and basified with 10% NaOH aq to pH > 12. The resulting precipitate was collected by filtration and dried *in vacuo* to afford **1** (1.82 g, 92%) as a tan solid. ^{1}H NMR (400 MHz, $CDCl_3$) δ: 7.50 (d, J = 8.8 Hz, 2H), 6.76 (d, J = 2.0 Hz, 2H), 6.70 (dd, J = 2.4, 8.8 Hz, 2H), 3.77 (br s, 4H).

*4.2.2. N-(7-Aminonaphthalen-2-yl)-4-methylbenzenesulfonamide (**2**).* A solution of tosyl chloride (270 mg, 1.4 mmol) in pyridine (10 mL) was added dropwise to a solution of 2,7-diaminonaphthalene **1** (158 mg, 1.0 mmol) in pyridine (5 mL) over 1 h at 0 °C. The reaction mixture was warmed to r.t. and stirred overnight before being quenched with water (100 mL). The resulting mixture was extracted with diethylether (100 mL), and the organic layer was acidified by 10% HCl aq. The separated aqueous layer was neutralized by NaOH aq. and extracted with diethylether (100 mL). The organic layer was dried over $MgSO_4$, filtered, and evaporated *in vacuo*. The resulting residue was used for next reactions without further purification as compound **2** (234 mg, 75%). Melting point: 156−158 °C; IR (KBr): 3406, 3339, 1636, 1516, 1346, 1320, 1159, and 1091 cm^{-1}; ^{1}H NMR (600 MHz, $CDCl_3$) δ: 7.67 (d, J = 8.3 Hz, 2H), 7.54 (dd, J = 6.8, 8.4 Hz, 2H), 7.27 (d, J = 1.8 Hz, 1H), 7.18 (d, J = 8.2 Hz, 2H), 6.92 (dd, J = 2.2, 8.6 Hz, 1H), 6.86 (dd, J = 2.2, 8.6 Hz, 1H), 6.83 (d, J = 1.9 Hz, 1H), 6.70 (br s, 1H), 3.87 (br s, 2H), 2.34 (s, 3H); ^{13}C{^{1}H}NMR (150 MHz, $CDCl_3$) δ: 144.9, 143.8, 136.1, 135.2, 134.5, 129.6 (2C), 129.1, 129.0, 127.2 (2C), 125.5, 117.7, 117.4, 116.3, 108.0, 21.5; HRMS (ESI) m/z [M + H]$^+$ calcd for $C_{17}H_{17}N_2O_2S$ 313.1011, found: 313.1007.

*4.2.3. 2,4-Bis(trifluoromethyl)benzo[g]quinolin-8-amine (**BQL**) and 1,3-Bis(trifluoromethyl)benzo[f]quinolin-9-amine (**BQA**).* Hexafluoroacetylacetone (1.4 mL, 9.7 mmol) and montmorillonite K10 (1.13 g) were added to a solution of compound **2** (755 mg, 2.42 mmol) in dry 1,4-dioxane (12 mL) under a N_2 atmosphere. The reaction mixture was stirred at 60 °C for 10 h under a N_2 atmosphere in an oil bath. The mixture was cooled to r.t. and filtered through celite, and the resulting filtrate was evaporated *in vacuo*. To this residue was added *conc*. H_2SO_4 (2.4 mL), and the resulting mixture was heated at 100 °C for 5 h in an oil bath. Following neutralization by NaOH aq., the mixture was extracted with AcOEt three times. The organic layer was dried over Na_2SO_4, filtered, and evaporated *in vacuo*. The residue was purified by silica gel column chromatography (*n*-hexane/AcOEt = 20/1) to afford **BQL** (38.0 mg, 5%) as a red solid and **BQA** (252 mg, 32%) as a yellow solid. Spectral data of **BQL**; melting point: 228−235 °C; IR (KBr): 3464, 3351, 1636, 1277, 1197, and 1135 cm^{-1}; ^{1}H NMR (600 MHz, $CDCl_3$) δ: 8.59 (s, 2H), 7.97 (d, J = 9.0 Hz, 1H), 7.82 (s, 1H), 7.17 (dd, J = 2.2, 8.9 Hz, 1H), 7.14 (d, J = 2.0 Hz, 1H), 4.22 (br s, 2H); ^{13}C{^{1}H}NMR (150 MHz, $CDCl_3$) δ: 147.4 (q, $^2J_{CF}$ = 35.6 Hz), 145.7, 144.5, 136.7 (q, $^2J_{CF}$ = 32.1 Hz), 136.6, 130.4, 129.4, 125.8, 123.7, 123.2 (q, $^1J_{CF}$ = 273.4 Hz), 122.7, 121.1 (q, $^1J_{CF}$ = 274.0 Hz), 118.1, 111.8, 105.2; ^{19}F{^{1}H}NMR (282 MHz, $CDCl_3$) δ: −62.8, −68.4; HRMS (ESI) m/z [M + H]$^+$ calcd for $C_{15}H_9F_6N_2$ 331.0669, found: 331.0707; anal. calcd for $C_{15}H_8F_6N_2$: C, 54.56; H, 2.44; N, 8.48. Found: C, 54.78; H, 2.60; N, 8.34.

Spectral data of **BQA**; melting point: 132−138 °C, IR (KBr): 3457, 3399, 1635, 1540, 1276, 1188, and 1137 cm^{-1}, ^{1}H NMR (300 MHz, $CDCl_3$) δ: 8.13 (s, 1H), 8.00−7.97 (m, 2H), 7.84 (d, J = 9.0 Hz, 1H), 7.79 (d, J = 8.5 Hz, 1H), 7.16 (dd, J = 2.1, 8.5 Hz, 1H), 4.13 (br, 2H); ^{13}C{^{1}H}NMR (150 MHz, $CDCl_3$) δ: 150.9, 146.3 (q, $^2J_{CF}$ = 35.6 Hz), 145.9, 135.3 (q, $^2J_{CF}$ = 32.6 Hz), 133.6, 130.2, 128.6, 126.9, 124.2, 123.9 (q, $^1J_{CF}$ = 273.5 Hz), 123.1, 121.2 (q, $^1J_{CF}$ = 273.3 Hz), 118.6, 114.8 (q, $^3J_{CF}$ = 7.2 Hz), 111.8 (q, $^3J_{CF}$ = 8.1 Hz); ^{19}F{^{1}H}-NMR (282 MHz, $CDCl_3$) δ: −58.0, −67.9; HRMS (ESI) m/z [M + H]$^+$ calcd for $C_{15}H_9F_6N_2$ 331.0669, found: 331.0705; anal. calcd for $C_{15}H_8F_6N_2$: C, 54.56; H, 2.44; N, 8.48. Found: C, 54.60; H, 2.47; N, 8.50.

*4.2.4. N-Phenyl-2,4-bis(trifluoromethyl)benzo[g]quinolin-8-amine (**BQL-Ph**) and N,N-Diphenyl-2,4-bis(trifluoromethyl)benzo-[g]quinolin-8-amine (**BQL-diPh**).* $Pd(OAc)_2$ (10 mg, 15 mol %), (t-Bu)$_3$P (8.7 mg, 15 mol %), and t-BuOK (64 mg, 0.6 mmol) were added to a solution of **BQL** (95 mg, 0.29 mmol) in dry toluene (3 mL), and this solution was degassed under a nitrogen atmosphere. The reaction mixture was heated in an oil bath and stirred at 100 °C for 8 h after bromobenzene (45 μL, 0.43 mmol) was added. The reaction mixture was cooled to room temperature, diluted with diethylether, and washed with water. The organic layer was dried over $MgSO_4$, filtered, and evaporated *in vacuo*. The resulting residue was purified by silica gel column chromatography (*n*-hexane/AcOEt = 200/1) to afford **BQL-Ph** (36 mg, 31%) and **BQL-diPh** (53 mg, 38%) as red solids.

Spectral data of **BQL-Ph**: melting point: 179−185 °C; IR (KBr): 3404, 1636, 1600, 1528, 1442, 1281, 1195, and 1139 cm^{-1}; ^{1}H NMR (600 MHz, $CDCl_3$) δ: 8.62 (s, 1H), 8.61 (br s, 1H), 8.02 (d, J = 9.1 Hz, 1H), 7.84 (s, 1H), 7.55 (d, J= 2.1 Hz, 1H), 7.44−7.38 (m, 3H),

https://dx.doi.org/10.1021/acs.joc.0c01878
J. Org. Chem. XXXX, XXX, XXX−XXX

7.29 (d, J = 7.4 Hz, 2H), 7.13 (t, J = 7.4 Hz, 1H), 6.15 (br s, 1H); $^{13}C\{^1H\}$NMR (150 MHz, $CDCl_3$) δ: 147.5 (q, $^2J_{CF}$ = 35.5 Hz), 144.6, 143.0, 141.1, 136.7 (q, $^2J_{CF}$ = 32.0 Hz), 136.4, 130.3, 130.1, 129.7 (2C), 126.6, 123.50, 123.47, 123.3, 123.1 (q, $^1J_{CF}$ = 273.2 Hz), 121.1 (q, $^1J_{CF}$ = 273.5 Hz), 120.3 (2C), 118.6, 112.1, 106.4; $^{19}F\{^1H\}$NMR (282 MHz, $CDCl_3$) δ: −61.9, −68.0; HRMS (ESI) m/z $[M + H]^+$ calcd for $C_{21}H_{13}F_6N_2$ 407.0983, found: 407.0980; anal. calcd for $C_{21}H_{12}F_6N_2$: C, 62.08; H, 2.98; N, 6.89. Found: C, 61.87; H, 3.06; N, 6.72.

Spectral data of **BQL-diPh**: melting point: 171−174 °C; IR (KBr): 1634, 1594, 1488, 1430, 1283, 1198, and 1124 cm^{-1}; ^1H NMR (600 MHz, $CDCl_3$) δ: 8.60 (s, 1H), 8.54 (s, 1H), 7.95 (d, J = 9.9 Hz, 1H), 7.84 (s, 1H), 7.49−7.46 (m, 2H), 7.37−7.33 (m, 4H), 7.23−7.20 (m, 4H), 7.18−7.15 (m, 2H); $^{13}C\{^1H\}$NMR (150 MHz, $CDCl_3$) δ: 147.4 (q, $^2J_{CF}$ = 35.5 Hz), 147.2, 146.7 (2C), 144.4, 136.6 (q, $^2J_{CF}$ = 32.5 Hz), 136.0, 130.6, 129.6 (4C), 129.5, 127.3, 126.6, 125.5 (4C), 124.5 (2C), 123.3, 123.1 (q, $^1J_{CF}$ = 273.3 Hz), 121.0 (q, $^1J_{CF}$ = 273.7 Hz), 119.2, 115.1, 112.4; $^{19}F\{^1H\}$NMR (282 MHz, $CDCl_3$) δ: −61.9, −68.0; HRMS (ESI) m/z $[M + H]^+$ calcd for $C_{27}H_{17}F_6N_2$ 483.1296, found: 483.1289; anal. calcd for $C_{27}H_{16}F_6N_2$: C, 67.22; H, 3.34; N, 5.81. Found: C, 67.38; H, 3.24; N, 5.77.

*4.2.5. N-Phenyl-1,3-bis(trifluoromethyl)benzo[f]quinolin-9-amine (**BQA-Ph**).* Pd(DPPF)Cl_2·CH_2Cl_2 (110 mg, 15 mol %), DPPF (80 mg, 15 mol %), and t-BuOK (100 mg, 0.9 mmol) were added to a solution of **BQA** (290 mg, 0.88 mmol) in dry 1,4-dioxane (5 mL), and this solution was degassed under a nitrogen atmosphere. The reaction mixture was heated in an oil bath and stirred at 100 °C for 10 h after bromobenzene (0.3 mL, 2.9 mmol) was added. The reaction mixture was cooled to room temperature, diluted with AcOEt, and washed with water. The organic layer was dried over Na_2SO_4, filtered, and evaporated *in vacuo*. The resulting residue was purified by silica gel column chromatography (n-hexane/AcOEt = 100/1) to afford **BQA-Ph** (220 mg, 62%) as an orange solid. Melting point: 129−132 °C; IR (KBr): 3415, 1620, 1596, 1540, 1498, 1274, 1192, and 1140 cm^{-1}; ^1H NMR (600 MHz, $CDCl_3$) δ: 8.31 (s, 1H), 8.12 (s, 1H), 8.00 (d, J = 8.9 Hz, 1H), 7.89 (d, J = 8.9 Hz, 1H), 7.85 (d, J = 8.6 Hz, 1H), 7.47 (dd, J = 2.1, 8.5 Hz, 1H), 7.40−7.35 (m, 2H), 7.25−7.22 (m, 2H), 7.11−7.07 (m, 1H), 6.10 (s, 1H); $^{13}C\{^1H\}$NMR (150 MHz, $CDCl_3$) δ: 150.9, 146.5 (q, $^2J_{CF}$ = 35.7 Hz), 143.4, 141.4, 135.4 (q, $^2J_{CF}$ = 32.6 Hz), 133.4, 130.1, 129.5 (2C), 128.6, 128.1, 125.0, 123.7 (q, $^1J_{CF}$ = 273.5 Hz), 123.4, 121.1 (q, $^1J_{CF}$ = 273.4 Hz), 120.0, 119.7 (2C), 120.0, 114.9 (q, $^3J_{CF}$ = 7.1 Hz), 113.6 (q, $^3J_{CF}$ = 7.7 Hz); $^{19}F\{^1H\}$NMR (282 MHz, $CDCl_3$) δ: −58.1, −67.5; HRMS (ESI) m/z $[M + H]^+$ calcd for $C_{21}H_{13}F_6N_2$ 407.0983, found: 407.0949; anal. calcd for $C_{21}H_{12}F_6N_2$: C, 62.08; H, 2.98; N, 6.89. Found: C, 62.05; H, 2.89; N, 7.00.

*4.2.6. N,N-Diphenyl-1,3-bis(trifluoromethyl)benzo[f]quinolin-9-amine (**BQA-diPh**).* $Pd(OAc)_2$ (2.2 mg, 10 mol %), $(t\text{-}Bu)_3P$ (4 mg, 20 mol %), and t-BuOK (33 mg, 0.3 mmol) were added to a solution of **BQA** (41 mg, 0.1 mmol) in dry toluene (1 mL), and this solution was degassed under a nitrogen atmosphere. The reaction mixture was heated in an oil bath and stirred at 100 °C for 3 h after bromobenzene (20 μL, 0.2 mmol) was added. The reaction mixture was cooled to room temperature, diluted with diethylether, and extracted with water. The organic layer was dried over $MgSO_4$, filtered, and evaporated *in vacuo*. The resulting residue was purified by silica gel column chromatography (n-hexane) to afford **BQA-diPh** (49 mg, 99%) as a yellow solid. Melting point: 146−148 °C; IR (KBr): 1615, 1595, 1523, 1496, 1271, 1189, and 1143 cm^{-1}; ^1H NMR (300 MHz, $CDCl_3$) δ: 8.25 (d, J = 1.7 Hz, 1H), 8.04 (s, 1H), 8.02 (d, J = 8.9 Hz, 1H), 7.92 (d, J= 8.9 Hz, 1H), 7.82 (d, J = 8.7 Hz, 1H), 7.58 (dd, J = 2.1, 8.7 Hz, 1H), 7.38−7.30 (m, 4H), 7.22−7.11 (m, 6H); $^{13}C\{^1H\}$NMR (150 MHz, $CDCl_3$) δ: 150.7, 147.7, 147.1 (2C), 146.6 (q, $^2J_{CF}$ = 35.8 Hz), 135.6 (q, $^2J_{CF}$ = 32.7 Hz), 133.3, 129.6 (4C), 129.5, 128.8, 128.3, 125.9, 125.4 (4C), 124.3, 124.2 (2C), 123.7, 123.3 (q, $^1J_{CF}$ = 273.4 Hz), 121.13 (q, $^2J_{CF}$ = 273.0 Hz), 121.08 (q, $^3J_{CF}$ = 8.0 Hz), 115.1 (q, $^3J_{CF}$ = 7.7 Hz); $^{19}F\{^1H\}$NMR (282 MHz, $CDCl_3$) δ: −58.9, −67.5; HRMS (ESI) m/z $[M + H]^+$ calcd for $C_{27}H_{17}F_6N_2$ 483.1296, found: 483.1288; anal. calcd for $C_{27}H_{16}F_6N_2$: C, 67.22; H, 3.34; N, 5.81. Found: C, 66.93; H, 3.48; N, 5.53.

4.3. Recrystallization. Recrystallizations of six **BQX** derivatives were performed at rt using the following solvents: **BQL** ($CHCl_3$), **BQL-Ph** (CH_3CN), **BQL-diPh** (CH_3CN), **BQA** (n-hexane/AcOEt), **BQA-Ph** (CH_2Cl_2/ether), and **BQA-diPh** (CH_2Cl_2/ether).

4.4. Single-Crystal X-ray Diffraction. X-ray reflection data were collected on a Rigaku R-AXIS RAPID II diffractometer and MicorMax-007HF with graphite monochromated Cu Kα radiation (λ = 1.54187 Å) at 93 ± 1 K. The molecular structures were solved using direct methods (SHELXL 97).[50] The crystallographic data file (cif.) in this paper has been deposited with the Cambridge Crystallographic Data Center (CCDC). The given parameters are summarized in Tables S1, S2, and Figures S44−S49.

4.5. Absorption and Emission Spectra and Fluorescent Quantum Yield Measurements. The solution samples (20 μM) for UV−vis absorption and fluorescence spectra were prepared using eight solvents (n-hexane, 1,4-dioxane, dibutylether, $CHCl_3$, AcOEt, n-butanol, acetonitrile, and MeOH). The solutions were placed in quartz cells (1 cm) and were bubbled by a nitrogen gas for 1 min before the measurements. The fluorescence spectra were acquired by excitation at the absorption maxima (440−450 nm for **BQL** derivatives and 400−450 nm for **BQA** derivatives) of **BQX**. The fluorescence quantum yields were calculated from fluorescence spectra measured in a calibrated integrating sphere system as absolute quantum yields.

4.6. Fluorescence Lifetime Measurements. The solution samples (20 μM) as mentioned above were also used for fluorescence lifetime measurements. The fluorescence decay plots were collected by a HORIBA FluoroCube using Ludox (Merck) for calibration. The obtained plots were analyzed by Das Analysis (HORIBA) to calculate the τ values by a linear fitting model with first-order exponential decay.

4.7. DFT Calculation.[39,42] Geometries of the studied molecules were optimized at the B3LYP/6-31G** level of theory using the 16A.03 revision of the Gaussian 16 program package. The all-optimized geometries were further confirmed as minima by carrying out frequency calculations. No imaginary frequencies were found. TD-DFT incorporating the Tamm−Dancoff approximation (TDA) calculations of the studied molecules for UV spectra were performed at the B3LYP/6-311G** level of theory. Bulk solvent effects (n-hexane) were evaluated using the integral equation formalism variant of the polarizable continuum model (IEFPCM). The D_{index} (the hole−electron distance and the charge-transfer length) and charge density difference (CCD) were derived from Gaussian output files and were calculated using Multiwfn to describe the ICT character quantitatively, in which the Iop (9/40 = 4) keyword was used to get more configuration coefficients.

4.8. pH Titrations of BQL and BQA Solutions. **BQL** and **BQA** were dissolved in 1,4-dioxane. To the **BQX** solutions were added the HCl solutions (>pH 2.0) or the McIlvaine buffer solutions (<pH 2.0),[43] and 25 μM solutions were prepared with different pH values (pH: 0.0−7.0). UV−vis spectra were conducted, and the change in absorptions was plotted as a function of the pH value. By a sigmoidal fitting, the pK_a values of the protonated-**BQL** and **BQA** were estimated to be 1.8 and 2.2, respectively.

4.9. Ammonia Responsiveness. **BQL** and **BQA** were diluted by KBr and mixed using a mortar and pestle for approximately 3 min, preparing the 2.0 wt % samples. The resulting mixed samples were exposed by an HCl gas that was prepared using a 33% HCl solution. After exposure for 10, 30, and 60 min, photos of the individual samples were taken. The resulting HCl salts after exposure for 60 min were exposed by an NH_3 gas that was prepared using a 28% NH_3 solution. After exposure for 5 s, the photos for the resulting samples were taken.

4.10. Cell Culture and Fluorescence Imaging of Hela Cells. HeLa cells were purchased from the Japanese Collection of Research Bioresources (JCRB) Cell Bank. HeLa cells were grown in Dulbecco's modified Eagle's medium (DMEM) including 10% fetal bovine serum (FBS), 4.5 g/L glucose, 100 units/mL penicillin, and 100 μg/mL streptomycin (Nacalai tesque) in a humidified atmosphere of 5% CO_2 at 37 °C. The cells were grown to confluence in 35 mm glass-based

https://dx.doi.org/10.1021/acs.joc.0c01878
J. Org. Chem. XXXX, XXX, XXX−XXX

dishes and treated with 10 μM **BQL** or **BQA** and 1000× of HCS LipidTOX Deep Red (Invitrogen) in DMEM before fluorescence imaging. The fluorescence signals from the live cells were captured by confocal laser microscopy (Nikon A1R). Excitation laser wavelengths were 403 nm for **BQA**, 488 nm for **BQL**, and 637 nm for LipidTOX Deep Red.

4.11. Evaluation of Photostability.[18,19] The compounds in methanol (20 μM, 2 mL) solution were placed into quartz cells with a stirring bar. These solutions were irradiated on the stirrer by a high-pressure Hg lamp (1000 W, Ushio) through a collecting lens. The reactions were followed by absorption spectrometry after irradiation (1, 2, 5, 10, 30, and 60 min).

4.12. Cell Culture and Differentiation Induction of 3T3-L1 Cells. 3T3-L1 cells were purchased from the JCRB (Japanese Collection of Research Bioresources) Cell Bank. 3T3-L1 cells were grown in DMEM including 10% FBS, 1.0 g/L glucose, 100 units/mL penicillin, and 100 μg/mL streptomycin in a humidified atmosphere of 5% CO_2 at 37 °C. The cells were grown in 35 mm glass-based dishes and differentiated by adding 3-isobutyl-1-methylxanthine (0.5 mM), insulin (10 μg/mL), and dexamethasone (1 μM) to the culture media incubated in a CO_2 incubator for three days. The media were replaced with other media including insulin (10 μg/mL), and cells were incubated in a CO_2 incubator for a further three days. The compounds (**BQL**, **BQL-Ph**, and **BQL-diPh**) in dimethyl sulfoxide (DMSO) solutions were diluted in culture media (1 μM) before fluorescence imaging. The bright-field and fluorescence images were captured by confocal laser microscopy (Nikon, A1R). Excitation laser wavelength at 488 nm and emission wavelength at 595 nm were used for fluorescence imaging.

4.13. MTS Assay. HeLa cells were dispensed into a 96-well plate at 5000 cells/well and incubated at 37 °C overnight. The compounds **BQL** and **BQA** in DMSO were diluted with a culture medium (100 μL/well) at several concentrations (n = 3) in the above-mentioned wells. The prepared plates were incubated at 37 °C for 2 h, washed with DMEM twice, and replaced with fresh DMEM containing FBS. These plates were incubated with CellTiter 96 (Promega, 10 μL/well) for 3 h at 37 °C before absorbance at 490 nm in each well was measured by Varioskan Flash (Thermo Scientific). The ratio of absorbance with nontreated wells was plotted as cell viability rates.

■ ASSOCIATED CONTENT

Supporting Information

The Supporting Information is available free of charge at https://pubs.acs.org/doi/10.1021/acs.joc.0c01878.

X-ray structures and the absorption and fluorescence spectra of **BQX**; fluorescence decay curves of **BQX**; DFT calculation results of **BQX**; pH titration of **BQL** and **BQA**; IR spectra change for solid **BQL** and **BQA**; Cartesian coordinates obtained from DFT calculation; cell imaging using **BQL**, **BQL-diPh**, **BQA**, and **BQA-diPh**; intracellular fluorescence spectra of **BQL** and **BQA**; cell viability assays of **BQL** and **BQA**; photostability of the MeOH solution of **BQL** and **BQA**; copies of the ^{1}H, ^{13}C, and ^{19}F NMR as well as IR spectra for **compound 2** and **BQX**; and thermal ellipsoid plots of crystal structures for **BQX** (PDF)

■ AUTHOR INFORMATION

Corresponding Authors

Yasufumi Fuchi − *Faculty of Pharmaceutical Sciences, Showa Pharmaceutical University, Machida 194-8543, Japan*; Email: fuchi@ph.bunri-u.ac.jp

Kazuteru Usui − *Faculty of Pharmaceutical Sciences, Showa Pharmaceutical University, Machida 194-8543, Japan*; orcid.org/0000-0002-2175-5221; Email: usui@ac.shoyaku.ac.jp

Satoru Karasawa − *Faculty of Pharmaceutical Sciences, Showa Pharmaceutical University, Machida 194-8543, Japan*; orcid.org/0000-0002-3107-442X; Email: karasawa@ac.shoyaku.ac.jp

Authors

Tomohiro Umeno − *Faculty of Pharmaceutical Sciences, Showa Pharmaceutical University, Machida 194-8543, Japan*

Yuichiro Abe − *Graduate School of Pharmaceutical Sciences, Kyushu University, Fukuoka 812-8582, Japan*; orcid.org/0000-0003-4283-8509

Keita Ikeno − *Faculty of Pharmaceutical Sciences, Showa Pharmaceutical University, Machida 194-8543, Japan*

Ryu Yamasaki − *Faculty of Pharmaceutical Sciences, Showa Pharmaceutical University, Machida 194-8543, Japan*; orcid.org/0000-0002-8976-2962

Iwao Okamoto − *Faculty of Pharmaceutical Sciences, Showa Pharmaceutical University, Machida 194-8543, Japan*

Complete contact information is available at: https://pubs.acs.org/10.1021/acs.joc.0c01878

Author Contributions

[§]Y.F. and T.U. contributed equally.

Author Contributions

S.K., conceptualization and completion of the original draft manuscript; I.O., reviewing and editing; Y.F., synthesis of molecules, spectral characterizations, X-ray analysis, all cell imaging, and partial writing; T.U., synthesis of molecules, spectral characterizations, all ammonia-responsiveness tests, and X-ray analysis; Y.A., conceptualization, synthesis of molecules, spectral characterizations, and X-ray analysis; K.I., partial spectral characterization; K.U., X-ray analysis, all DFT calculations; R.Y., VT-NMR and reviewing and editing.

Notes

The authors declare no competing financial interest.

■ ACKNOWLEDGMENTS

This work was supported by a Grant-in-Aid for Scientific Research (C) (Grant Numbers 19K07016 for S.K. and 17K08212 for Y.F.) from the Japan Society for Promotion Sciences (JSPS) and a Grant-in-Aid for Young Scientists of Showa Pharmaceutical University (T.U.). Y.F. also acknowledges support from the Takeda Science Foundation. The authors thank Dr. K. Hamada and Prof. A. Mizutani of Showa Pharmaceutical University for valuable advice related to 3T3-L1 cells. The computations were performed at the Research Institute for Information Technology, Kyushu University.

■ REFERENCES

(1) Lakowics, J. R. *Principles of Fluorescence Spectroscopy*; 3rd ed.; Springer Science+Business Media: New York, 2006; pp 63−95.

(2) Gonçalves, M. S. T. Fluorescent Labeling of Biomolecules with Organic Probes. *Chem. Rev.* **2009**, *109*, 190−212.

(3) Stalin, T.; Rajendiran, N. Intramolecular Charge Transfer Effects on 3-Aminobenzoic Acid. *Chem. Phys.* **2006**, *322*, 311−322.

(4) Yang, Z.; Cao, J.; He, Y.; Yang, J. H.; Kim, T.; Peng, X.; Kim, J. S. Macro-/Micro-Environment-Sensitive Chemosensing and Biological Imaging. *Chem. Soc. Rev.* **2014**, *43*, 4563−4601.

(5) Martinez, V.; Henary, M. Nile Red and Nile Blue: Applications and Syntheses of Structural Analogues. *Chem. − Eur. J.* **2016**, *22*, 13764−13782.

(6) Yamaguchi, E.; Wang, C.; Fukazawa, A.; Taki, M.; Sato, Y.; Sasaki, Y.; Ueda, M.; Sasaki, N.; Higashiyama, T.; Yamaguchi, S. Environment-Sensitive Fluorescent Probe: A Benzophosphole Oxide

https://dx.doi.org/10.1021/acs.joc.0c01878
J. Org. Chem. XXXX, XXX, XXX−XXX

with an Electron-Donating Substituent. *Angew. Chem., Int. Ed.* **2015**, *54*, 4539−4543.
(7) Tirinato, L.; Pagliari, F.; Limongi, T.; Marini, M.; Falqui, A.; Seco, J.; Candeloro, P.; Liberale, C.; Di Fabrizio, E. An Overview of Lipid Droplets in Cancer and Cancer Stem Cells. *Stem Cells Int.* **2017**, *2017*, 1−17.
(8) Beckman, M. Great Balls of Fat. *Science* **2006**, *311*, 1232−1234.
(9) Fletcher, A. N. Quinine Sulfate as a Fluorescence Quantum Yield Standard. *Photochem. Photobiol.* **1969**, *9*, 439−444.
(10) Yamazawa, S.; Nakashima, M.; Suda, Y.; Nishiyabu, R.; Kubo, Y. 2,3-Naphtho-Fused BODIPYs as Near-Infrared Absorbing Dyes. *J. Org. Chem.* **2016**, *81*, 1310−1315.
(11) Vollmer, F.; Rettig, W.; Birckner, E. Photochemical Mechanisms Producing Large Fluorescence Stokes Shifts. *J. Fluoresc.* **1994**, *4*, 65−69.
(12) Kopchuk, D. S.; Chepchugov, N. V.; Starnovskaya, E. S.; Khasanov, A. F.; Krinochkin, A. P.; Santra, S.; Zyryanov, G. V.; Das, P.; Majee, A.; Rusinov, V. L.; Charushin, V. N. Synthesis and Optical Properties of New 2-(5-Arylpyridine-2-yl)-6-(het)arylquinoline-based "Push-Pull" Fluorophores. *Dyes Pigm.* **2019**, *167*, 151−156.
(13) Abe, Y.; Karasawa, S.; Koga, N. Crystal Structures and Emitting Properties of Trifluoromethylaminoquinoline Derivatives: Thermal Single-Crystal-to-Single-Crystal Transformation of Polymorphic Crystals That Emit Different Colors. *Chem. − Eur. J.* **2012**, *18*, 15038−15048.
(14) Karasawa, S.; Hagihara, R.; Abe, Y.; Harada, N.; Todo, J.; Koga, N. Crystal Structures, Thermal Properties, and Emission Behaviors of *N*,*N*-R-Phenyl-7-amino-2,4-trifluoromethylquinoline Derivatives: Supercooled Liquid-to-Crystal Transformation Induced by Mechanical Stimuli. *Cryst. Growth Des.* **2014**, *14*, 2468−2478.
(15) Karasawa, S.; Todo, J.; Usui, K.; Harada, N.; Yoza, K.; Suemune, H.; Koga, N. Regioselective Photocyclizations of Di(quinolinyl)arylamines and Tri(quinolinyl)amine with Emission Color Changes and Photoreaction-Induced Self-Assemblies. *Chem. − Eur. J.* **2016**, *22*, 7771−7781.
(16) Hagihara, R.; Usui, K.; Karasawa, S. Two-step Transformation of *p*-Anisolylaminoquinoline Derivatives Induced by Conformation- and Packing-Dominated Processes. *Dyes Pigm.* **2017**, *143*, 401−408.
(17) Hirota, J.; Usui, K.; Fuchi, Y.; Sakuma, M.; Matsumoto, S.; Hagihara, R.; Karasawa, S. Fluorescence Properties and Exciplex Formation of Emissive Naphthyridine Derivatives: Application as Sensors for Amines. *Chem. − Eur. J.* **2019**, *25*, 14943−14952.
(18) Fuchi, Y.; Sakuma, M.; Ohyama, K.; Hagihara, R.; Kohno, M.; Hamada, K.; Mizutani, A.; Karasawa, S. Selective Synthesis of Substituted Amino-Quinoline Derivatives by C-H Activation and Fluorescence Evaluation of Their Lipophilicity-Responsive Properties. *Sci. Rep.* **2019**, *9*, No. 17723.
(19) Sakuma, M.; Fuchi, Y.; Usui, K.; Karasawa, S. Photophysical Properties of Emissive Pyrido[3,2-*c*]carbazole Derivatives and Apoptosis Induction: Development towards Theranostic Agents in Response to Light Stimulus. *Chem. Asian J.* **2019**, *14*, 3938−3945.
(20) Araki, T.; Murayama, S.; Usui, K.; Shimada, T.; Aoki, I.; Karasawa, S. Self-Assembly Behavior of Emissive Urea Benzene Derivatives Enables Heat-Induced Accumulation in Tumor Tissue. *Nano Lett.* **2017**, *17*, 2397−2403.
(21) Prochorow, J.; Deperasińska, I.; Stepanenko, Y. Fluorescence Excitation and Fluorescence Spectra of Jet-Cooled Phenanthridine and 7,8-Benzoquinoline. *Chem. Phys. Lett.* **2004**, *399*, 239−246.
(22) Karim, M.; Jahng, Y. Unusual Product Distribution from Friedländer Reaction of Di- and Triacetylbenzenes with 3-Aminonaphthalene-2-carbaldehyde and Properties of New Benzo[*g*]quinoline-Derived Aza-aromatics. *Molecules* **2014**, *19*, 12842−12851.
(23) Taniya, O. S.; Kopchuk, D. S.; Khasanov, A. F.; Kovalev, I. S.; Santra, S.; Rahman, M.; Zyryanov, G. V.; Majee, A.; Charushin, V. N.; Chupakhin, O. N. 2-Azaanthracenes: A Chronology of Synthetic Approaches and Bright Prospects for Practical Applications. *New J. Chem.* **2019**, *43*, 11382−11390.
(24) Zou, Y.; Young, D. D.; Cruz-Montanez, A.; Deiters, A. Synthesis of Anthracene and Azaanthracene Fluorophores *via* [2+2+2] Cyclotrimerization Reactions. *Org. Lett.* **2008**, *10*, 4661−4664.
(25) Kopchuk, D. S.; Chepchugov, N. V.; Taniya, O. S.; Khasanov, A. F.; Giri, K.; Kovalev, I. S.; Santra, S.; Zyryanov, G. V.; Majee, A.; Rusinov, V. L.; Chupakhin, O. N. 3-Cyano-2-azaanthracene-based 'Push-Pull" Fluorophores: A One-step Preparation from 5-Cyano-1,2,4-triazines and 2,3-Dehydronaphthalene, Generated in situ. *Tetrahedron Lett.* **2016**, *57*, 5639−5643.
(26) Zhang, P.; Chu, H.; Li, X.; Feng, W.; Deng, P.; Yuan, L.; Gong, B. A New Method for Aromatic Difluoromethylation: Copper-Catalyzed Cross-Coupling and Decarboxylation Sequence from Aryl Iodides. *Org. Lett.* **2011**, *13*, 54−57.
(27) Yamashkin, S. A.; Yudin, L. G.; Kost, A. N. Closure of the Pyridine Ring in the Combes Quinoline Synthesis. *Chem. Heterocycl. Compd.* **1992**, *28*, 845−855.
(28) Cannon, J. G.; Born, J. L.; Krunnfusz, R. W. Preparation of benzo[g]quinolines from 1-methyl-5,6-dimethoxy-2-naphthylamine. *J. Heterocycl. Chem.* **1972**, *9*, 959−962.
(29) Cui, Y-J.; Su, F.; Jin, W.-J. Structural and Luminescent Properties of Co-crystals of Tetraiodoethylene with Two Azaphenanthrenes. *Acta Crystallogr., Sect. E: Cryst. Commun.* **2020**, *76*, 438−442.
(30) Gattu, R.; Basha, R. S.; Bagdi, P. R.; Khan, A. T. One-pot Three-Component Regioselective Synthesis of C1-Functionalised 3-Arylbenzo[*f*]quinolone. *RSC Adv.* **2016**, *6*, 11675−11682.
(31) Corey, E. J.; Rohde, J. J.; Fischer, A.; Azimioara, M. D. A Hypothesis for Conformational Restriction in Complexes of Formyl Compounds with Boron Lewis acids. Experimental Evidence for Formyl CH–O and CH–F Hydrogen Bonds. *Tetrahedron Lett.* **1997**, *38*, 33−36.
(32) Andrews, D. P.; Beddard, G. S.; Whitaker, B. J. Charge-Transfer Formation and Geometry of the Naphthalene−Trimethylamine van der Waals Complex. *J. Phys. Chem. A* **2000**, *104*, 7785−7792.
(33) Carlotti, B.; Flamini, R.; Kikaš, I.; Mazzucato, U.; Spalletti, A. Intramolecular Charge Transfer, Solvatochromism and Hyperpolarizability of Compounds Bearing Ethenylene or Ethynylene Bridges. *Chem. Phys.* **2012**, *407*, 9−19.
(34) Density functional theory (DFT) calculations were performed at the B3LYP/6-31G** level.
(35) Weigert, F. J.; Mahler, W. NMR Parameters of the Individual Fluorines of the Trifluoromethyl Group. *J. Am. Chem. Soc.* **1972**, *94*, 5314−5318.
(36) Mei, J.; Leung, N. L. C.; Kwok, R. T. K.; Lam, J. W. Y.; Tang, B. Z. Aggregation-Induced Emission: Together We Shine, United We Soar! *Chem. Rev.* **2015**, *115*, 11718−11940.
(37) Kim, S.; Fujitsuka, M.; Tohnai, N.; Tachikawa, T.; Hisaki, I.; Miyata, M.; Majima, T. The Unprecedented J-Aggregate Formation of Rhodamine Moieties Induced by 9-Phenylanthracenyl Substitution. *Chem. Commun.* **2015**, *51*, 11580−11583.
(38) Lu, T.; Chen, F. Multiwfn: A multifunctional Wavefunction Analyzer. *J. Comput. Chem.* **2012**, *33*, 580−592.
(39) Liu, S.; Lu, J.; Lu, Q.; Fan, J.; Lin, L.; Wang, C.; Song, Y. Theoretical Study on the Sensing Mechanism of Novel Hydrazine Sensor TAPHP and Its ESIPT and ICT Processes. *Front. Chem.* **2020**, *7*, 932.
(40) The S_r index indicates the overlap degree of hole and electron (the theoretical upper limit is 1.0).
(41) The *t* index indicates the separation of hole and electron. The *t* index > 0 means that there is significant separation of hole and electron.
(42) Adamo, C.; Bahers, T. L.; Savarese, M.; Wilbraham, L.; García, G.; Fukuda, R.; Ehara, M.; Rega, N.; Ciofini, I. Photo-induced Redox Catalysis for Proton Reduction to Hydrogen with Homogeneous Molecular Systems Using Rhodium-Based Catalysts. *Coord. Chem. Rev.* **2015**, *304*−*305*, 20−37.
(43) McIlvaine, T. C. A Buffer Solution for Colorimetric Comparison. *J. Biol. Chem.* **1921**, *49*, 183−186.
(44) Coin, I.; Beyermann, M.; Bienert, M. Solid-phase Peptide Synthesis: from Standard Procedures to the Synthesis of Difficult Sequences. *Nat. Protoc.* **2007**, *2*, 3247−3256.

https://dx.doi.org/10.1021/acs.joc.0c01878
J. Org. Chem. XXXX, XXX, XXX−XXX

(45) Umeno, T.; Ueda, A.; Doi, M.; Kato, T.; Oba, M.; Tanaka, M. Helical Foldamer-Catalyzed Enantioselective 1,4-Addition Reaction of Dialkyl Malonates to Cyclic Enones. *Tetrahedron Lett.* **2019**, *60*, No. 151301.
(46) Xu, H.; Zhang, H.; Liu, G.; Kong, L.; Zhu, X.; Tian, X.; Zhang, Z.; Zhang, R.; Wu, Z.; Tian, Y.; Zhou, H. Coumarin-Based Fluorescent Probes for Super-resolution and Dynamic Tracking of Lipid Droplets. *Anal. Chem.* **2019**, *91*, 977−982.
(47) Adler, J.; Parmryd, I. Quantifying Colocalization: the MOC Is a Hybrid Coefficient − an Uninformative Mix of Co-occurrence and Correlation. *Cytometry, Part A* **2010**, *77A*, 733−742.
(48) Ghosh, C.; Nandi, S.; Bhattacharyya, K. Probing Micro-Environment of Lipid Droplets in a Live Breast Cell: MCF7 and MCF10A. *Chem. Phys. Lett.* **2017**, *670*, 27−31.
(49) Novikoff, A. B.; Novikoff, P. M.; Rosen, O. M.; Rubin, C. S. Organelle Relationships in Cultured 3T3-L1 Preadipocytes. *J. Cell Biol.* **1980**, *87*, 180−196.
(50) Scheldrick, G. M.; Schneider, T. R. SHELX97: High-Resolution Refinement. In *Methods in Enzymology*; Academic Press, 1997; Vol. *277*, pp 319−343.

https://dx.doi.org/10.1021/acs.joc.0c01878
J. Org. Chem. XXXX, XXX, XXX−XXX